Supplementary Information

"Broken-Hearted" Carbon Bowl via Electron Shuttle Reaction: Energetics and Electron Coupling

Gabrielle A. Leith,[‡a] Allison M. Rice,[‡a] Brandon J. Yarbrough,[a] Preecha Kittikhunnatham,[a] Abhijai Mathur,[a] Nicholas A. Morris,[a] Megan J. Francis,[a] Anna A. Berseneva,[a] Poonam Dhull,[a] Richard D. Adams,[a] M. Victoria Bobo,[a] Aaron A. Vannucci,[a] Mark D. Smith,[a] Sophya Garashchuk,[a] and Natalia B. Shustova*[a]

[a]*Department of Chemistry and Biochemistry, University of South Carolina, Columbia, South Carolina 29208, United States*

Table of Contents: **page number**

Materials. 2,7-dihydroxynaphthalene (99%, Chem-Impex International, Inc.), *N,N*-diethylcarbamoyl chloride (99%, Acros Organics), pyridine (99+%, Alfa Aesar), dichloro(1,3-bis(diphenylphosphino)propane)nickel (99%, Ark Pharm, Inc), methylmagnesium bromide (ACS grade, Alfa Aesar), diethyl ether (HPLC grade, Fisher Scientific), aluminum bromide (99%, Strem Chemicals, Inc.), oxalyl chloride (98%, Alfa Aesar), dichloromethane (ACS grade, Macron), Girard′s Reagent T (99%, Acros Organics), acetic acid (ACS grade, Fisher Scientific), methyl ethyl ketone (99.9%, Oakwood Chemical), 3-hexanone (>98%, Tokyo Chemical Industry Co, LTD), potassium hydroxide (ACS grade, Fisher Scientific), methanol (HPLC grade, Fisher Scientific), 2,5-norbornadiene (97%, Alfa Aesar), acetic anhydride (99%, Chem-Impex International, Inc.), cyclohexane (reagent grade, Malinckrodt), silica gel (Macron), *N*-bromosuccinimide (96%, Oakwood Chemical), benzoyl peroxide (97%, Sigma-Aldrich), carbon tetrachloride (ACS grade, Fisher Scientific), 1,4-dioxane (99+%, Alfa Aesar), sodium hydroxide (ACS grade, Fisher Scientific), zinc (97.5%, BeanTown Chemical), potassium iodide (ACS grade, Fisher Scientific), ethanol (200 proof, Decon Laboratories, Inc.), 7,7,8,8-tetracyanoquinodimethane (98%, Alfa Aesar), mercury(II) chloride (ACS grade, Sigma-Aldrich), sodium carbonate (ACS grade, Macron), tetrakis(triphenylphosphine)palladium(0) (98%, Matrix Scientific), sodium bicarbonate (ACS grade, Macron), hexane (ACS grade, BDH), hydrochloric acid (ACS grade, EMD Chemicals), tetrahydrofuran (ACS grade, EMD Chemicals), acetonitrile (HPLC grade, Fisher Scientific), anhydrous magnesium sulfate (reagent grade, J.T. Baker® Chemicals), corning Pyrex glass tubing (O.D. = ½”), lithium bromide (99+%, Chem-Impex International, Inc.), 1,3-dimethylurea (98%, Acros Organics), tripyrrolidinophosphine oxide (98%, Tokyo Chemical Industry Co, LTD), *N,N*-dimethylformamide (HPLC grade, Fisher Scientific), tetrahydrofuran (HPLC grade, Fisher Scientific), sodium metal (99.95%, Alfa Aesar), anhydrous ammonia (99+%, Praxair), chloroform-*d* (Cambridge Isotope Laboratories, Inc.), and DMSO-d_6 (Cambridge Isotope Laboratories, Inc.) were used as received. Compounds **I**–**V** were prepared according to a modified literature procedure.[1,2]

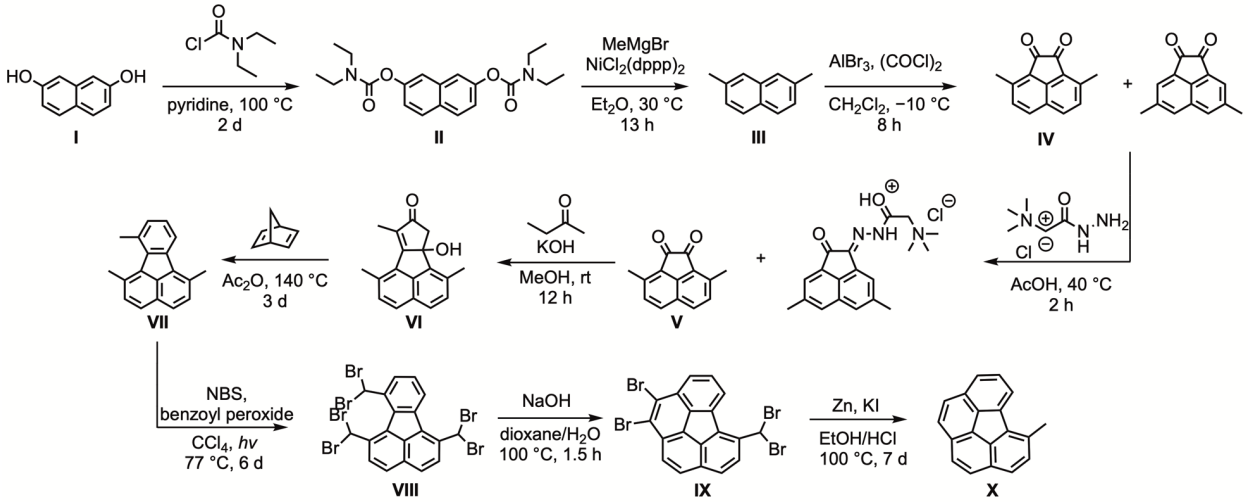

Scheme S1. Synthesis of 5-methylbenzo[*ghi*]fluoranthene (**X**).

The products (**X** and **X′**) and several precursors were characterized by ^{1}H and ^{13}C NMR spectroscopy and mass spectrometry (Figures S18–S21). For the synthesis of the "open" corannulene analogs, instead of 3-pentanone utilized for traditional corannulene preparation,1 we used 2-butanone (route 1, step 5, Scheme S1) and 3-hexanone (route 2, step 5, Scheme S2). We were able to isolate and characterize the products: 1,6,7-trimethylfluoranthene (**VII**, Scheme S1, Figure S18) and 7-ethyl-1,6,10-trimethylfluoranthene (**VII'**, Scheme S2, Figure S19) by single-crystal X-ray diffraction in addition to spectroscopic analysis. The lack of a methyl group (Scheme S1 and Figure S24) and additional ethyl group (Scheme S2 and Figure S25) on the fluoranthene core, in comparison with the corannulene synthesis, allowed us to close only one side of the ring, resulting in formation of 5-methylbenzo[*ghi*]fluoranthene ($C_{19}H_{12}$, **X**) and 5-ethyl-6-methylbenzo[*ghi*]fluoranthene ($C_{21}H_{16}$, **X'**), respectively. Sublimation of the produced yellow powder (**X**, Scheme S1) in a sealed ampule at 200 °C allowed for the formation of single-crystals of **X** suitable for X-ray diffraction (Figure S24). The structure of **X'** was confirmed based on ^{1}H and ^{13}C NMR spectroscopy and mass spectrometry analysis (Figure S21). As in the case of the solid-state "open" P-$C_{20}H_{14}$, both **X** and **X'** structures possess a planar geometry (Figures S24 and S25).

7-dihydro-8*H*-cyclopenta[*a*]acenaphthylene-8-one ($C_{18}H_{16}O_2$ (VI), Scheme S1).

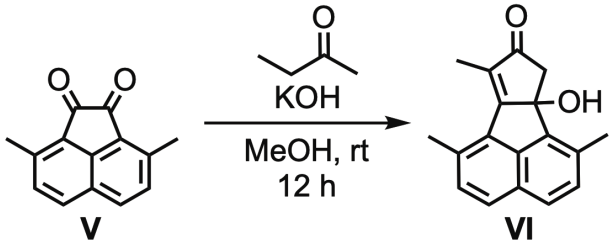

Potassium hydroxide (0.35 g, 6.2 mmol) was dissolved in dry methanol (0.64 mL, 16 mmol) in a 5-mL Schlenk flask purged with nitrogen. Then, methyl ethyl ketone (0.22 mL, 2.5 mmol) and 3,8-dimethylacenaphthylene-1,2-dione (**V**, 54 mg, 0.26 mmol) were added to the flask under a nitrogen flow. The resulting mixture was stirred at room temperature for 12 hours and then the mixture was diluted with equal volume of water. The desired compound was extracted from the aqueous layer using dichloromethane (3 × 10 mL). The combined organic layers were neutralized with hydrochloric acid (1 mL, 3 M), washed with water (3 × 10 mL), and dried using magnesium sulfate. Dichloromethane was removed under reduced pressure, resulting in a brown oil (0.042 g), which was used without further purification.

1,6,7-trimethylfluoranthene ($C_{19}H_{16}$ (VII), Scheme S1).

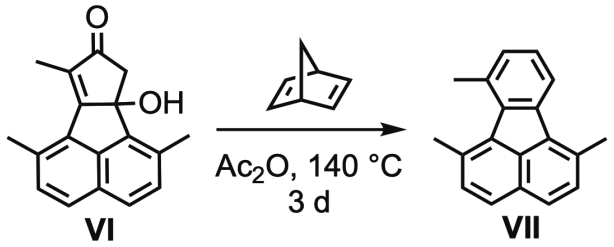

Norbornadiene (0.18 mL, 1.8 mmol), 7-dihydro-8*H*-cyclopenta[*a*]acenaphthylen-8-one (**VI**, 54 mg, 0.26 mmol), and acetic anhydride (2.2 mL, 23 mmol) were added in a 5-mL round bottom flask. The reaction mixture was heated at 140 °C for three days, cooled down to room temperature, and then a solution of sodium hydroxide (2.2 mL, 10 wt%) was added to quench the excess of acetic anhydride. The desired compound was extracted from the aqueous layer with dichloromethane (3 × 10 mL). The combined organic layers were washed with water (3 × 10 mL), dried using magnesium sulfate, and then dichloromethane was removed under reduced pressure. The resulting product was purified by column chromatography using cyclohexane to give 1,6,7-trimethylfluoranthene (**VII**, 35 mg, 68%) as a yellow solid. Single crystals of **VII** were obtained

by slow evaporation of a saturated cyclohexane solution at room temperature. The detailed description for the crystallographic data collection and refinement details are given in Table S1. ^{1}H NMR ($CDCl_3$, 300 MHz): δ = 7.89 (1H, d, J = 7.5), 7.71–7.67 (2H, m), 7.38–7.28 (3H, m), 7.17 (1H, d, J = 7.6), 2.99 (3H, s), 2.90 (3H, s) and 2.89 (3H, s). ^{13}C NMR ($CDCl_3$, 101 MHz) δ = 141.08, 141.07, 139.01, 135.40, 133.39, 133.12, 132.98, 132.91, 132.89, 132.43, 130.74, 130.65, 127.04, 126.68, 126.11, 121.37, 25.64, 25.50, and 20.98 ppm (Figure S18). HRMS (EI, m/z) calculated for $C_{19}H_{16}$ $[M+H]^+$ 244.1303, found 244.1306.

1,6,7-tris(dibromomethyl)fluoranthene ($C_{19}H_{10}Br_6$ (VIII), Scheme S1).

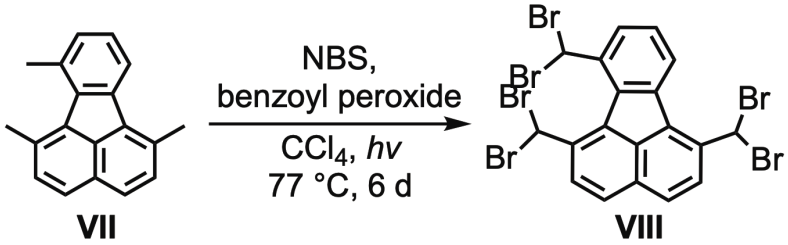

Benzoyl peroxide (8.1 mg, 0.033 mmol), 1,6,7-trimethylfluoranthene (**VII**, 0.86 g, 3.5 mmol), *N*-bromosuccinimide (5.9 g, 33 mmol), and carbon tetrachloride (69 mL, 0.71 mol) were added in a 100-mL Schlenk flask purged with nitrogen. The reaction mixture was heated at 77 °C while irradiated with a 300 W lamp for six days. The solvent was removed under reduced pressure, and the obtained powder (1.4 g, 54%) was used without further purification.

1,2-dibromo-6-(bromomethyl)benzo[*ghi*]fluoranthene ($C_{19}H_8Br_4$ (IX), Scheme S1).

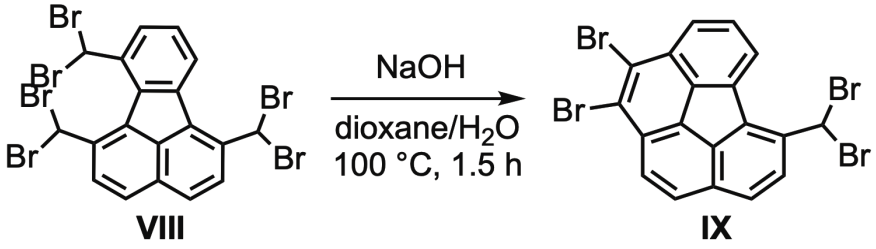

Sodium hydroxide pellets (24 mg, 0.59 mmol), 1,6,7-tris(dibromomethyl)fluoranthene (**VIII**, 51 mg, 0.071 mmol), dioxane (2.0 mL, 23 mmol), and water (0.79 mL, 44 mmol) were added in a 50-mL round bottom flask. The resulting mixture was heated at 100 °C for one and a half hours, cooled down to room temperature, followed by the addition of equal volume of water,

and neutralized using 3 M hydrochloric acid. The precipitate was filtered, washed with water, and dried under reduced pressure. The resulting product was isolated with 27% yield (15 mg) and was used without further purification. HRMS (EI, m/z) calculated for $[C_{19}H_8Br_4+H]^+$: 555.7320, found 555.7321.

5-methylbenzo[*ghi*]fluoranthene ($C_{19}H_{12}$ (X), Scheme S1).

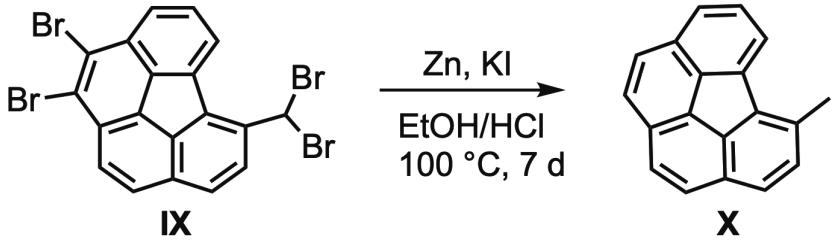

Zinc (0.71 g, 11 mmol), 1,2-dibromo-6-(bromomethyl)benzo[*ghi*]fluoranthene (**IX**, 59 mg, 0.11 mmol), potassium iodide (0.25 g, 1.5 mmol), ethanol (10 mL, 0.18 mol), and 4% hydrochloric acid (0.59 mL, 16 mmol) were added in a 15-mL round bottom flask. The reaction mixture was heated at 100 °C for seven days. Once the reaction mixture cooled to room temperature, solvent was removed under reduced pressure. The crude product was purified by a Soxhlet extraction procedure using dichloromethane as the solvent. The solvent was removed under reduced pressure, and the product was isolated as a yellow solid (**X**, 13 mg, 52 %). Sublimation of **X** in a sealed ampule at 200 °C allowed for the formation of single crystals. The detailed description for the crystallographic data collection and refinement details are given in Table S1. ^{1}H NMR ($CDCl_3$, 400 MHz): δ = 8.14 (1H, d, J = 7.0), 7.99–7.84 (6H, m), 7.71 (1H, t, J = 7.5), 7.48 (1H, d, J = 8.1), 2.97 (3H, s). ^{13}C NMR ($CDCl_3$, 101 MHz): δ = 136.29, 131.37, 128.22, 127.65, 126.78, 126.72, 126.71, 126.61, 126.55, 126.49, 126.45, 126.08, 126.01, 125.99, 125.88, 125.14, 124.24, 125.05, and 19.91 (Figure S20). HRMS (EI, m/z) calculated for $[C_{19}H_{12}+H]^+$: 240.0939, found 240.0942.

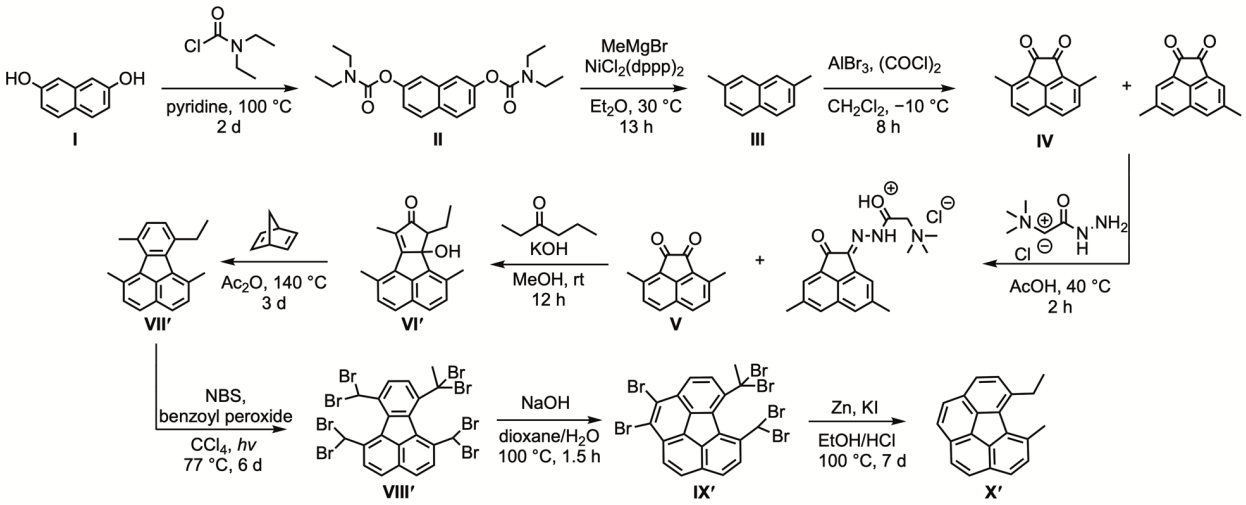

Scheme S2. Synthesis of 5-ethyl-6-methylbenzo[*ghi*]fluoranthene (**X′**).

7-ethyl-6b-hydroxy-1,6,9-trimethyl-6b,7-dihydro-8*H*-cyclopenta[*a*]acenaphthylen-8-one ($C_{20}H_{20}O_2$ (VI′), Scheme S2).

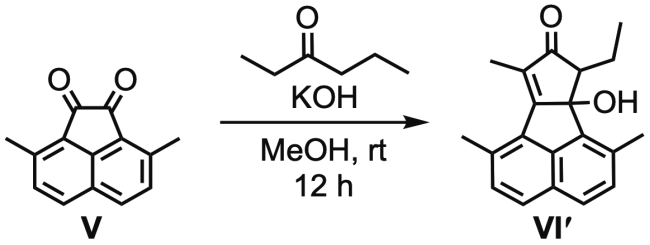

Potassium hydroxide (0.35 g, 6.2 mmol) was dissolved in dry methanol (0.64 mL, 16 mmol) in a 5-mL Schlenk flask purged with nitrogen. Then, 3-hexanone (0.24 mL, 2.5 mmol) and 3,8-dimethylacenaphthylene-1,2-dione (**V**, 0.054 g, 0.26 mmol) were added to the flask under a nitrogen flow. After that, the resulting mixture was stirred for 12 hours at room temperature. Then, the mixture was diluted with an equal volume of water and the desired compound was extracted from the aqueous layer using dichloromethane (3 × 10 mL). The combined organic layers were neutralized with hydrochloric acid (1 mL, 3 M), washed with water (3 × 10 mL), dried using magnesium sulfate, and dichloromethane was removed under reduced pressure, resulting in a brown oil (0.051 g), which was used without further purification.

7-ethyl-1,6,10-trimethylfluoranthene ($C_{21}H_{20}$ (VII′), Scheme S2).

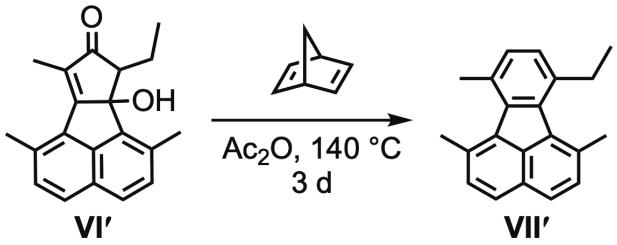

Norbornadiene (0.18 mL, 1.8 mmol), 7-ethyl-6b-hydroxy-1,6,9-trimethyl-6b,7-dihydro-8*H*-cyclopenta[*a*]acenaphthylen-8-one (**VI′**, 0.075 g, 0.26 mmol), and acetic anhydride (2.2 mL, 23 mmol) were added in a 5-mL round bottom flask. The resulting mixture was heated at 140 °C for three days, cooled down to room temperature, and a sodium hydroxide solution (2.2 mL, 10 wt%) was added to quench excess of acetic anhydride. The desired compound was extracted from the aqueous layer with dichloromethane (3 × 10 mL), washed with water (3 × 10 mL), and dried using magnesium sulfate. Dichloromethane was removed under reduced pressure. The resulting crude product was purified by column chromatography using cyclohexane to give 7-ethyl-1,6,10-trimethylfluoranthene (**VII′**, 57 mg, 81%) as a yellow powder. Single crystals of **VII′** were obtained by slow evaporation of a saturated cyclohexane solution at room temperature. The detailed description for the crystallographic data collection and refinement details are given in Table S1. ^{1}H NMR ($CDCl_3$, 300 MHz): δ = 7.68 (2H, d, J = 8.3), 7.37 (2H, dd, J = 8.3, 2.7), 7.19 (2H, sext, J = 6.3), 3.13 (2H, q, J = 7.5), 2.84 (3H, s), 2.81 (3H, s), 2.75 (3H, s), and 1.31 (3H, t, J = 7.5) ppm. ^{13}C NMR ($CDCl_3$, 101 MHz): δ = 139.89, 138.98, 136.45, 134.90, 134.83, 133.54, 131.97, 131.74, 131.69, 130.75, 129.51, 128.26, 126.51, 126.32, 126.02, 125.91, 28.46, 24.95, 24.63, 24.16, and 15.63 ppm (Figure S19). HRMS (EI, m/z): calculated for $[C_{21}H_{20}]^+$ 272.1565, found 272.1567.

7-(1,1-dibromoethyl)-1,6,10-tris(dibromomethyl)fluoranthene ($C_{21}H_{12}Br_8$ (VIII′), Scheme S2).

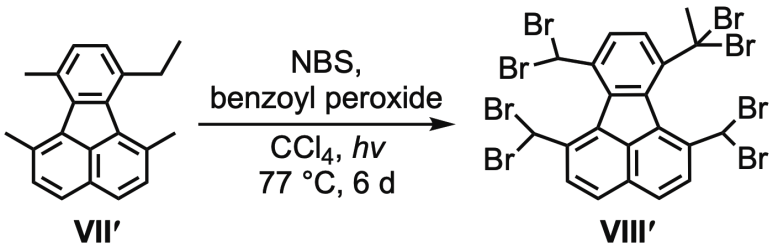

Benzoyl peroxide (0.35 mg, 0.0015 mmol), 7-ethyl-1,6,10-trimethylfluoranthene (**VII′**) (0.040 g, 0.15 mmol), *N*-bromosuccinimide (0.26 g, 2.1 mmol), and carbon tetrachloride (3.0 mL, 31 mmol) were added to a 5-mL Schlenk flask purged with nitrogen. The reaction mixture was heated at 77 °C while irradiated with a 300 W lamp for six days. After that, the solvent was removed under reduced pressure, and the solid was purified by a Soxhlet extraction procedure using ethanol as the solvent resulting in a brown powder (70 mg, 52%), which was used without further purification.

1,2-dibromo-5-(1,1-dibromoethyl)-6-(dibromomethyl)benzo[*ghi*]fluoranthene ($C_{21}H_{10}Br_6$ (IX′), Scheme S2).

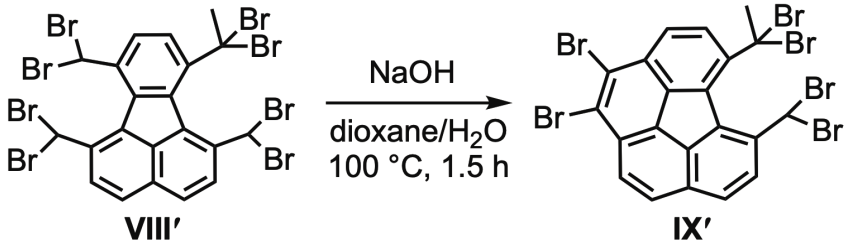

Sodium hydroxide (0.12 g, 3.0 mmol), 7-(1,1-dibromoethyl)-1,6,10-tris(dibromomethyl)fluoranthene (**VIII′**, 0.025 g, 0.030 mmol), dioxane (3 mL, 35 mmol), and water (1 mL, 56 mmol) were added in a 10-mL round bottom flask. The reaction mixture was heated at 100 °C for one and a half hours, cooled down to room temperature, followed by the addition of water (4 mL), and neutralized using 3 M hydrochloric acid. The obtained precipitate was filtered, washed with water, and dried under reduced pressure. The resulting product (17 mg, 82%) was then used without further purification.

5-ethyl-6-methylbenzo[*ghi*]fluoranthene ($C_{21}H_{16}$ (X′), Scheme S2).

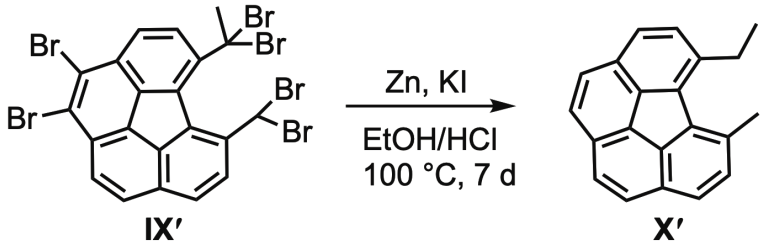

IX′ **X′**

Zinc powder (0.36 g, 5.5 mmol), 1,2-dibromo-6-(bromomethyl)benzo[*ghi*]fluoranthene (**IX′**, 0.040 g, 0.053 mmol), potassium iodide (0.13 g, 0.78 mmol), ethanol (5.0 mL, 0.090 mol), and 4% hydrochloric acid (0.29 mL, 8.0 mmol) were added in a 10-mL round bottom flask. The reaction mixture was heated at 100 °C for seven days, cooled down to room temperature, and the solvent was removed under reduced pressure. The crude product was purified by a Soxhlet extraction procedure using dichloromethane as the solvent. The solvent was removed under reduced pressure and the product was isolated as a yellow powder (6.7 mg, 47 %). ^{1}H NMR ($CDCl_3$, 400 MHz): δ = 7.86 (1H, d, J = 8.6), 7.78-7.68 (5H, m), 7.65 (1H, d, J = 8.5), 7.49 (1H, d, J = 7.8), 2.78 (3H, s), 2.48 (2H, q, J = 7.4), and 0.98 (3H, t, J = 7.4) ppm. ^{13}C NMR ($CDCl_3$, 101 MHz): δ = 136.80, 135.96, 135.91, 135.69, 135.59, 134.76, 131.50, 130.95, 130.88, 130.52, 130.40, 127.06, 127.05, 126.99, 126.86, 126.69, 126.61, 125.74, 30.31, 27.48, and 18.82 ppm (Figure S21). HRMS (EI, m/z): calculated for $[C_{21}H_{16}]^+$ 268.1252, found 268.1249.

$C_{20}H_{10}$·$C_{20}H_{14}$·$C_{12}H_4N_4$ ($C_{52}H_{28}N_4$, 1).

A mixture of corannulene ($C_{20}H_{10}$, 15 mg, 0.060 mmol), 7,7,8,8-tetracyanoquinodimethane (TCNQ, 14 mg, 0.068 mmol), and zinc powder (50 mg, 0.76 mmol) was ground together followed by the addition of 3 μL of 12 M hydrochloric acid. Then, the resulting mixture was placed in a borosilicate glass ampule (diameter = 12.7 mm; length = 130 mm), which was flame-sealed under vacuum (4×10^{-5} mbar). The tube was placed in a sand bath at 200 °C, and the top end of the tube was wrapped with a piece of aluminum foil. After six days, brown rod-like crystals (**1**) formed (conversion yield 18%). Since the reaction is clean and there are only unreacted byproducts (e.g., corannulene), the conversion yield was determined based on the amount of starting material (corannulene) that was converted to the product (P-$C_{20}H_{14}$). The obtained crystals were suitable for single-crystal X-ray analysis (Figure S1 and S2 and Table S1). Table S1 contains crystallographic refinement data for **1**. More detailed description of the crystal structure can be

found in the *X-ray Crystal Structure Determination section* (vide infra). The mass spectrometry (MS) data is shown in Figure S3. The epifluorescence microscopy image of **1** and an emission spectrum of **1** collected from a single crystal are shown in Figure S5. Parent corannulene and TCNQ were also studied using the epifluorescence microscopy and photoluminescence spectroscopy (Figure S5).

$(C_{20}H_{10})_2 \cdot C_{12}H_4N_4$ ($C_{52}H_{24}N_4$, (corannulene)$_2 \cdot$ TCNQ).

A mixture of corannulene (15 mg, 0.060 mmol) and TCNQ (14 mg, 0.068 mmol) was ground together. Then, the resulting mixture was placed in a borosilicate glass ampule (diameter = 12.7 mm; length = 130 mm), which was flame-sealed under vacuum (4×10^{-5} mbar). The tube was placed in a sand bath at 200 °C, and the top end of the tube was wrapped with aluminum foil.

After six days, brown rod-like crystals were formed. The obtained crystals were suitable for single-crystal X-ray analysis and match closely to the reported crystal structure.[3] The MS spectroscopic data are shown in Figure S4.

$C_{16}H_{10} \cdot C_{12}H_4N_4 \cdot$ ($C_{28}H_{14}N_4$, pyr·TCNQ).

The pyrene and TCNQ (pyr·TCNQ) co-crystals were prepared according to a modified literature procedure.[4] Pyrene (0.010 g, 0.050 mmol) and TCNQ (0.010 g, 0.050 mmol) were heated at reflux in a benzene/toluene mixture (1 mL / 1 mL) for two hours in a 5-mL round bottom flask. The reaction mixture was cooled to room temperature and after one day of slow evaporation of the solvent, black crystals were obtained. The obtained crystals were suitable for single-crystal X-ray analysis (Figure S17). Table S1 contains crystallographic refinement data for $C_{16}H_{10} \cdot C_{12}H_4N_4$. More detailed description of the crystal structure can be found in the *X-ray Crystal Structure Determination section* (vide infra).

$C_{14}H_{10}·C_{12}H_4N_4$·($C_{26}H_{14}N_4$, phenan·TCNQ).

The phenanthrene and TCNQ (phenan·TCNQ) co-crystals were prepared according to a modified literature procedure.[4] Phenanthrene (13 mg, 0.074 mmol) and TCNQ (15 mg, 0.074 mmol) were ground together, and the resulting mixture was placed in a borosilicate glass ampule (diameter = 12.7 mm; length = 130 mm) before flame-sealing under vacuum (4×10^{-5} mbar). The tube was then placed in a sand bath at 200 °C with the top end of the tube wrapped with aluminum foil. After six days, brown rod-like crystals were isolated, and match closely to the reported crystal structure.[4]

Solution reactions.

A series of reactions were investigated in solution in attempts to repeat the results of the reduction reaction that occurred with corannulene in a sealed ampule. Starting with relatively lower boiling point solvents, such as dichloromethane and methanol, the same equivalents of the reagents were used (i.e., corannulene, TCNQ, Zn, and HCl), and heated at reflux in the solvent for six days. No evidence of the planar 5,6-dimethyl-benzo[*ghi*]fluoranthene was found through ^{1}H NMR spectroscopy or mass spectrometry. In order to more closely match the successful high temperature (200 °C) reaction conditions resulting in the formation of **1**, solvents such as ethylene glycol (b.p. = 197 °C) and glycerol (b.p. = 290 °C) were used. In this case, no evidence of the planar 5,6-dimethyl-benzo[*ghi*]fluoranthene was also found through ^{1}H NMR spectroscopy or mass spectrometry.

In order to investigate if the type of electron shuttle used could make a difference in solution-based reactions, TCNQ, which was used in the formation of **1**, was replaced with methyl viologen, another common electron shuttle.[5] Using the same conditions as above, still no product was observed through ^{1}H NMR spectroscopy and mass spectrometry.

In addition, the reducing agent (zinc) was replaced with sodium dithionite under the aforementioned reaction conditions, and there was no evidence of product formation.

In addition, we explored the Clemmensen reduction since it utilizes similar reagents (zinc and hydrochloric acid) to transform corannulene using a modified literature procedure.[6] As a first step, zinc amalgam was prepared by combining zinc dust (29 mg, 0.44 mmol), mercury(II) chloride (2.5 mg, 9.2 μmol), and 0.13 mL of 3.5% hydrochloric acid in a round-bottom flask and stirred for five minutes. To a 10-mL round bottom flask, corannulene (25 mg, 0.10 mmol), ethanol (3 mL),

and the prepared zinc amalgam were added. Finally, concentrated hydrochloric acid (2 mL) was added and the reaction mixture was heated at 80 °C for 3 days. The solvent was removed under reduced pressure and the residue was extracted with ethyl acetate (3 × 10 mL). The combined organic layers were washed with water (3 × 10 mL), dried over sodium sulfate, and then solvent was removed under reduced pressure. The resulting yellow oil was revealed to be corannulene based on ^{1}H NMR spectroscopy and mass spectrometry.

Electrochemical reactions.

An electrochemical Birch reduction was pursued to hydrogenate or cleave a C=C bond based on a literature procedure.[7] To a glass cell vial, corannulene (15 mg, 0.060 mmol), lithium bromide in anhydrous THF (1.5 M, 3 mL), tripyrrolidinophosphine oxide (0.135 mL), 1,3-dimethylurea (5.3 mg, 0.060 mmol), and 1.8 mL of anhydrous THF were added. A magnesium electrode as the anode and stainless steel as the cathode were submerged in the solution and the resulting solution was purged with nitrogen for five minutes. Using Aftermath software, a chronopotentiometry experiment was set up and 10 mA was applied for 24 h (see Physical Measurements for more details). Then the solution was transferred to a round bottom flask and solvent was removed under reduced pressure. Diethyl ether (10 mL) and a saturated solution of sodium tartrate (10 mL) were added to the flask and stirred overnight. The solution was then extracted with diethyl ether (3 × 15 mL), and the combined organic layers were washed with water (3 × 15 mL). The organic layers were dried over magnesium sulfate and solvent was removed under reduced pressure to produce a yellow oil. The oil was analyzed and found only corannulene based on ^{1}H NMR spectroscopy and mass spectrometry.

X-ray Crystal Structure Determination.

Single-Crystal X-ray Structure of $C_{20}H_{10}\cdot C_{20}H_{14}\cdot C_{12}H_4N_4$ ($C_{52}H_{28}N_4$, 1).

X-ray intensity data from a dark brown needle were collected at 100(2) K using a Bruker D8 QUEST diffractometer equipped with a PHOTON-100 CMOS area detector and an Incoatec microfocus source (Mo Kα radiation, λ = 0.71073 Å). All of several crystals screened were found to be twinned by non-merohedry. From the crystal judged to be the best quality, all reflections from a trial set of 569 could be indexed to two domains using the Cell_Now program.[8] Orientation matrices for the two domains along with the twin law relating the domains were also derived using

Cell_Now. The twin law is (-1 0 0.147 / 0 -1 0 / 0 0 1), corresponding to a two-fold rotation around the real-space [001] axis. The raw area detector data frames were reduced, scaled, and corrected for absorption effects using the Bruker APEX3, SAINT+, and TWINABS programs.[8] The reported unit cell parameters were determined by least-squares refinement of 8512 reflections taken from both domains. The structure was solved by direct methods with SHELXT.[9] Subsequent difference Fourier calculations and full-matrix least-squares refinement against F^2 were performed with SHELXL-2014[10] using OLEX2.[11] The major twin domain volume fraction refined to 0.633(3).

The compound crystallizes in the triclinic system. The space group *P*–1 (No. 2) was confirmed by structure solution. The asymmetric unit consists of one $C_{20}H_{10}$ (corannulene) molecule, one $C_{20}H_{14}$ molecule, and half each of two $C_{12}H_4N_4$ (TCNQ) molecules. Both TCNQ molecules are located on crystallographic inversion centers. The corannulene molecule is disordered and was modeled with two orientations (A/B). The disorder takes the form of a near-180° rotation around an axis perpendicular to the central five-membered ring. Total group occupancy was constrained to sum to unity and refined to A/B = 0.611(5)/0.389(5). Similar sets of bonds between the two components were restrained to have approximately the same distances, using SHELX SADI instructions. These are: the two sets of five bonds each of the central C5 rings (e.g., C1–C2), the two sets of five bonds radiating from each central C5 ring (e.g., C1–C6), the two sets of five bonds outermost in each phenyl ring (e.g., C7–C8), and the remaining two sets of ten phenyl C–C bonds (e.g., C6–C7, C8–C9). Some atoms which appear nearly superimposed were assigned equal displacement parameters. In total 367 restraints were used in the disorder modeling. All non-hydrogen atoms were refined with anisotropic displacement parameters. Most hydrogen atoms bonded to carbon, including the methyl hydrogens of the $C_{20}H_{14}$ molecule, were located in Fourier difference maps before being placed in geometrically idealized positions and included as riding atoms (d(C–H) = 0.95 Å and U_{iso}(H) = 1.2U_{eq}(C) for aromatic hydrogen atoms and d(C–H) = 0.98 Å and U_{iso}(H) = 1.5U_{eq}(C) for methyl hydrogens). The methyl hydrogens were allowed to rotate as a rigid group to the orientation of maximum observed electron density. Anti-bumping restraints (d(H–H) > 2.0 Å) were applied to two sets of H atoms, H50A–H8B and H50A–H49C. The largest residual electron density peak in the final difference map is 0.43 e/Å^3, located 1.13 Å from H49A. This peak and the next highest peak lie between C49 and C50 and, though small in magnitude, were considered carefully. Ultimately, no reasonable alternative molecular model

could be achieved; they most likely arise from a minor whole-molecule disorder component of this species.

Single-Crystal X-ray Structure of 1,6,7-trimethylfluoranthene ($C_{19}H_{16}$, VII).

X-ray intensity data from a colorless needle were collected at 100(2) K using a Bruker D8 QUEST diffractometer equipped with a PHOTON-100 CMOS area detector and an Incoatec microfocus source (Mo Kα radiation, λ = 0.71073 Å). The raw area detector data frames were reduced and corrected for absorption effects using the Bruker APEX3, SAINT+, and SADABS programs.[8] The structure was solved with SHELXT.[9] Subsequent difference Fourier calculations and full-matrix least-squares refinement against F^2 were performed with SHELXL-2018[10] using OLEX2.[11]

The compound crystallizes in the orthorhombic system. The pattern of systematic absences in the intensity data was uniquely consistent with the space group $P2_12_12_1$, which was confirmed by structure solution. The asymmetric unit consists of one molecule. All non-hydrogen atoms were refined with anisotropic displacement parameters. Hydrogen atoms bonded to carbon were located in difference Fourier maps before being placed in geometrically idealized positions and included as riding atoms with d(C–H) = 0.95 Å and U_{iso}(H) = 1.2U_{eq}I for aromatic hydrogen atoms and d(C–H) = 0.98 Å and U_{iso}(H) = 1.5I(C) for methyl hydrogens. The methyl hydrogens were allowed to rotate as a rigid group to the orientation of maximum observed electron density. The largest residual electron density peak in the final difference map is 0.19 e/Å^3, located 1.11 Å from C3.

Single-Crystal X-ray Structure of 7-ethyl-1,6,10-trimethylfluoranthene ($C_{21}H_{20}$, VII′).

X-ray intensity data from a colorless block were collected at 100(2) K using a Bruker D8 QUEST diffractometer equipped with a PHOTON-100 CMOS area detector and an Incoatec microfocus source (Mo Kα radiation, λ = 0.71073 Å). The raw area detector data frames were reduced and corrected for absorption effects using the Bruker APEX3, SAINT+, and SADABS programs.[8] The structure was solved with SHELXT.[9] Subsequent difference Fourier calculations and full-matrix least-squares refinement against F^2 were performed with SHELXL-2018[10] using OLEX2.[11]

The compound crystallizes in the orthorhombic system. The pattern of systematic absences

in the intensity data was consistent with the space groups *Pnma* and $Pna2_1$. The acentric group $Pna2_1$ was assigned by the solution program XT and was confirmed by structure solution. The asymmetric unit consists of one molecule. All non-hydrogen atoms were refined with anisotropic displacement parameters. Hydrogen atoms bonded to carbon were located in difference Fourier maps before being placed in geometrically idealized positions and included as riding atoms with d(C–H) = 0.95 Å and U_{iso}(H) = 1.2U_{eq}(C) for aromatic hydrogen atoms, d(C–H) = 0.99 Å and U_{iso}(H) = 1.2U_{eq}(C) for methylene hydrogen atoms, and d(C–H) = 0.98 Å and U_{iso}(H) = 1.5U_{eq}(C) for methyl hydrogens. The methyl hydrogens were allowed to rotate as a rigid group to the orientation of maximum observed electron density. The largest residual electron density peak in the final difference map is 0.56 e/Å^3, located 0.72 Å from H19B. Because of the absence of heavy atoms in the crystal, Friedel opposites were merged during refinement and no attempt was made to determine the absolute structure.

Single-Crystal X-ray Structure of 5-methylbenzo[*ghi*]fluoranthene ($C_{19}H_{12}$, X).

Crystals formed as pale-yellow blocks. During screening, the diffraction patterns of several specimens showed strong low-angle diffraction diminishing rapidly in intensity at higher θ. The observed d_{max} was > 1 Å for all samples surveyed. This is caused by severe whole-molecule disorder within the crystals (see below). X-ray intensity data collected at 100(2) K using a Bruker D8 QUEST diffractometer equipped with a PHOTON-100 CMOS area detector and an Incoatec microfocus source (Mo Kα radiation, λ = 0.71073 Å). The raw area detector data frames were reduced and corrected for absorption effects using the Bruker APEX3, SAINT+ and SADABS programs.[8] An initial structural solution was obtained with SHELXT.[9] Subsequent difference Fourier calculations and full-matrix least-squares refinement against F^2 were performed with SHELXL-2018[10] using OLEX2.[11]

The compound crystallizes in the monoclinic system. The pattern of systematic absences in the intensity data was uniquely consistent with the space group $P2_1/c$. The asymmetric unit consists of two molecules. Initial solutions returned two independent regions of planar, nearly circular concentrations of electron density peaks, corresponding to the two molecules. No single, ordered molecule was evident among these nearly featureless disks of disordered peaks. Several disorder models were undertaken, beginning with two orientations of the target molecule per independent molecular site. This proved insufficient to account for the observed electron density

and resulted in R_1-values greater than 17.5%. A somewhat improved model incorporated a third molecular orientation per site, though R_1-values are still high (*ca*. 15%). Molecular site occupancies were constrained to sum to one, and refined to: C1–C19(A/B/C) = 0.626(4)/0.310(4)/0.064(4) and C21–C39(A/B/C) = 0.570(4)/0.362(4)/0.068(4). Many restraints were necessary for the disorder modeling (total 1734 from 1918 data and 795 parameters). The C–C distances were restrained values similar to those found in the few planar benzofluoranthene structures reported in the literature. Further distance restraints were necessary to maintain six-membered ring geometries close to hexagonal (all opposite C–C distances per ring were restrained to be similar). Non-hydrogen atoms were refined with anisotropic displacement parameters except for the minor components of each independent molecule (atom label suffixes "C"). These were refined with a common isotropic displacement parameter for each molecule. All displacement parameters were restrained using an enhanced rigid-bond restraint (SHELX RIGU). Some nearly superimposed atoms were given equal anisotropic displacement parameters. Some disorder components were restrained to planarity using SHELX FLAT. Hydrogen atoms bonded to carbon were placed in geometrically idealized positions and included as riding atoms with d(C–H) = 0.95 Å and U_{iso}(H) = 1.2U_{eq}(C) for aromatic hydrogen atoms and d(C–H) = 0.98 Å and U_{iso}(H) = 1.5U_{eq}(C) for methyl hydrogens. The largest residual electron density peak in the final difference map is 0.42 e/Å^3, located 0.46 Å from C12C. The absence of high-angle data due to the weak diffraction coupled with the extensive whole-molecule disorder requiring a large set of parameters results in a poor data-to-parameter ratio and an approximate, heavily restrained structural model.

Single-Crystal X-ray Structure of $C_{16}H_{10}\cdot C_{12}H_4N_4$, ($C_{28}H_{14}N_4$, pyr·TCNQ).

X-ray intensity data from a dark brown plate were collected at 100(2) K using a Bruker D8 QUEST diffractometer equipped with a PHOTON-100 CMOS area detector and an Incoatec microfocus source (Mo Kα radiation, λ = 0.71073 Å). The raw area detector data frames were reduced and corrected for absorption effects using the Bruker APEX3, SAINT+ and SADABS programs.[8] Final unit cell parameters were determined by least-squares refinement of 9208 reflections taken from the data set. The structure was solved with SHELXT.[9] Subsequent difference Fourier calculations and full-matrix least-squares refinement against F^2 were performed with SHELXL-2018[10] using OLEX2.[11]

The compound crystallizes in the monoclinic system. The pattern of systematic absences

in the intensity data was consistent with the space group $P2_1/n$, which was confirmed by structure solution. The asymmetric unit consists of half of one pyrene molecule and half of one TCNQ molecule, both located on crystallographic inversion centers. All non-hydrogen atoms were refined with anisotropic displacement parameters. Hydrogen atoms bonded to carbon were located in Fourier difference maps and refined freely. The largest residual electron density peak in the final difference map is 0.23 e/Å^3, located 0.72 Å from C3.

Table S1. X-ray structure refinement data for **1,** pyr·TCNQ, $C_{19}H_{16}$, $C_{21}H_{20}$, and $C_{19}H_{12}$.[a]

compound	**1**	pyr·TCNQ	$C_{19}H_{16}$	$C_{21}H_{20}$	$C_{19}H_{12}$
formula	$C_{52}H_{28}N_4$	$C_{28}H_{14}N_4$	$C_{19}H_{16}$	$C_{21}H_{20}$	$C_{19}H_{12}$
FW	708.78	406.43	244.32	272.37	240.29
T, K	100(2)	100(2)	100(2)	100(2)	100(2)
crystal system	triclinic	monoclinic	orthorhombic	orthorhombic	monoclinic
space group	*P*–1	$P2_1/n$	$P2_12_12_1$	$Pna2_1$	$P2_1/c$
Z	2	2	4	4	8
a, Å	10.5126(12)	6.9885(3)	5.0524(4)	9.8601(4)	18.410(3)
b, Å	13.2993(15)	10.0688(4)	15.7417(11)	9.0281(4)	11.5059(17)
c, Å	13.3298(15)	14.6611(5)	15.7910(11)	16.8983(6)	12.1836(18)
α, °	88.442(3)	90	90	90	90
β, °	84.692(3)	103.5890(10)	90	90	109.148(4)
γ, °	69.641(3)	90	90	90	90
V, Å^3	1739.7(3)	1002.76(7)	1255.91(16)	1504.3(10)	2438.1(6)
d_{calc}, g/cm^3	1.353	1.346	1.292	1.203	1.309
μ, mm^{-1}	0.080	0.082	0.073	0.068	0.074
F(000)	736.0	420.0	520.0	548.0	1008.0
crystal size, mm^3	0.4 × 0.06 × 0.06	0.16 × 0.12 × 0.06	0.22 × 0.06 × 0.04	0.18 × 0.14 × 0.08	0.22 × 0.10 × 0.08
theta range	4.47 to 50.052	4.954 to 55.126	5.16 to 50.088	5.116 to 55.106	4.684 to 37.68
index ranges	−12 ≤ h ≤ 12 −15 ≤ k ≤ 15 0 ≤ l ≤ 15	−9 ≤ h ≤ 8 −13 ≤ k ≤ 13 −19 ≤ l ≤ 18	−6 ≤ h ≤ 6 −17 ≤ k ≤ 18 −18 ≤ l ≤ 18	−12 ≤ h ≤ 12 −11 ≤ k ≤ 11 −21 ≤ l ≤ 21	−16 ≤ h ≤ 16 −10 ≤ k ≤ 10 −11 ≤ l ≤ 11
Refl. collected	6143	20689	16295	62323	17727
data/restraints/ parameters	6143/367/666	2306/0/174	2212/0/176	3461/1/194	1918/1734/795
GOF on F^2	1.019	1.037	1.065	1.054	2.103
R_1/wR_2, $[I \geq 2\sigma(I)]^b$	0.0622/0.1365	0.0376/0.0856	0.0451/0.0924	0.0490/0.1159	0.1492/0.4106

[a]Mo-K$_\alpha$ (λ= 0.71073Å) radiation
[b]$R_1 = \Sigma||F_o| - |F_c||/ \Sigma |F_o|$, $wR_2 = \{\Sigma [w(F_o^2-F_c^2)^2]/ \Sigma [w(F_o^2)^2]\}^{1/2}$

Physical measurements.

An Edinburgh FS5 fluorescence spectrometer equipped with a 150 W Continuous Wave Xenon Lamp source for excitation was used to acquire steady-state emission spectra. Emission measurements on solutions were measured using a standard cuvette holder (SC-05) and measurements were collected in quartz cuvettes in THF. In addition, emission measurements on single crystals were collected on an Ocean Optics UV-4000 spectrometer connected to an epifluorescence microscope using a 450 μm SMA fiber optic cable. Epifluorescence microscope images were collected on an Olympus BX51 microscope equipped with a 120 W mercury vapor short arc excitation light source. An Ocean Optics JAZ spectrometer was used for diffuse reflectance measurements with an Ocean Optics ISP-REF integrating sphere connected to the spectrometer using a 450 μm SMA fiber optic cable. The samples were placed in a 6.0 mm quartz sample cell with a cover and placed on top of the integrating sphere. An Ocean Optics WS-1 Spectralon® reference standard was placed on the sample cell throughout the measurements. Absorption spectra were collected on a PerkinElmer Lambda 35 UV-vis spectrometer. FTIR spectra were collected on a PerkinElmer Spectrum 100. A WaveDriver 20 Bipotentiostat combined with Aftermath software was employed to carry out bulk electrolysis experiments in anhydrous *N,N*-dimethylformamide as well as chronopotentiometry experiments in anhydrous tetrahydrofuran. NMR spectra were obtained on a Bruker Avance III-HD 300 and Bruker Avance III 400 MHz NMR spectrometers. ^{13}C and ^{1}H NMR spectra were referenced to natural abundance ^{13}C peaks and residual ^{1}H peaks of deuterated solvents, respectively. A VG70S magnetic sector mass spectrometer was used to record the mass spectra of the prepared compounds. Sample introduction was by direct probe with electron ionization (EI) at 70 eV.

Computational details.

The electronic structure calculations were performed using density functional theory (DFT), specifically the B3LYP functional paired with the 6-31G* basis to optimize the geometry and with 6-311+G** to obtain the excited electronic states, unless otherwise noted. For the latter, the Grimme′s dispersion correction has been invoked and the electronic excitations analysis is based on the time-dependent density functional theory (TDDFT) with the random phase approximation (RPA).[12] The electronic structure method for geometry optimization has been selected after additional calculations, including the ground state geometry optimization of $C_{20}H_{12}$

at the MP2 and CCSD level using 6-31+G* and cc-pVDZ bases, that yielded marginal differences in geometry compared to the DFT results. Selected excited state calculations were performed using the LRC-ωPBEh density functional and, for experimentally relevant molecular models TCNQ and TCNQ/$C_{20}H_{10}$, yielded electronic excitations at slightly higher energies (by about 0.15 eV or 3-5%). All calculations were performed using Spartan16 and Q-Chem 5.2 software.[13,14]

As the primary driving force of corannulene flattening, we considered corannulene strain energy. Based on an extensive literature analysis, we found a strain energy database for various polycyclic aromatic hydrocarbons (PAHs) among which extended carbon π-bowls were presented.[15] Cheng and coworkers computationally estimated strain energy (E_s) as a nonplanar distortion (E_{np}), i.e., Es = E_{np} Eqn (S1).

$$E_{\mathrm{np}} = \eta \times \Sigma \frac{m}{m+1} \text{ (S1)}$$

where η = 418.4 kJ/mol, the sum ($\Sigma \frac{m}{m+1}$) is over vertexes of a PAH, and m can be estimated as:

$$m = \frac{2 \sin^2\left(\theta_{\sigma\pi} - \frac{\pi}{2}\right)}{\left(1 - 3 \sin^2\left(\theta_{\sigma\pi} - \frac{\pi}{2}\right)\right.} \text{ (S2)}$$

where $\theta_{\sigma\pi}$ = the solid angle made by the π-orbital axis vector (POAV) commonly used as a parameter for estimation of molecule's curvature and it can be directly calculated from the molecule coordinates.[16,17] According to this equation (Eqn(S1)), strain energy for planar PAH can be estimated as 0 kJ/mol since every vertex possess the parameter $\theta_{\sigma\pi} = \pi/2$, consequently, m = 0 and hence E_{np} and E_s are equal to 0 kJ/mol.

The standard enthalpy changes during the C=C breaking process in Eqn (S3):

$$C_{20}H_{10} + 2H_2 \rightarrow C_{20}H_{14} \text{ (S3)}$$

is −179.5 kJ/mol. The electronic and the zero-point vibrational energies (ZPE) are –239 and 60 kJ/mol, respectively. Additional data on the energies are given in Table S2. Therefore, from a thermodynamics point of view, this process is not favorable, and we probed a possible driving force for this process – strain energy. We attempted to estimate how much energy is released due to strain energy during the planarization of corannulene as a result of the C=C bond breaking process (E'). The electronic component of released energy (E') was computed as the energy

difference of the π-bowl energy with only the methyl units relaxed, and that of the fully relaxed P-$C_{20}H_{14}$ and was determined to be 202 kJ/mol (Figure S9).

Table S2. Electronic and zero-point vibrational energies (ZPE), and the total enthalpy at standard temperature and pressure (298 K, 1 atm). All geometries are optimized; the methods are B3LYP/6-31+G* and LRC-ωPBEh/6-31+G*.

Species	B3LYP			LRC- ωPBEh		
	E_{el}, a.u.	ZPE, kJ/mol	H^0, kJ/mol	E_{el}, a.u.	ZPE, kJ/mol	H^0, kJ/mol
$C_{20}H_{10}^{curved}$	–768.1727	608.449	641.206	–767.392	616.387	648.968
H_2	–1.17548	26.660	36.556	–1.1671	26.752	35.430
$C_{20}H_{14}$	–770.6147	721.301	759.701	–769.8266	729.376	769.525
$C_{20}H_{10}^{planar}$	–768.1578	607.550	644.240	–767.3763	615.052	645.905
$\Delta_{rxn} = C_{20}H_{14} - 2H_2 - C_{20}H_{10}^{curved}$; $\Delta_{inv} = C_{20}H_{10}^{planar} - C_{20}H_{10}^{curved}$ (all in kJ/mol)						
Δ_{rxn}	–239.03	59.532	45.383	–263.60	59.485	49.697
Δ_{inv}	39.120	–0.899	3.0340	41.220	–1.335	–3.063

Similarly to the calculated strain energy from literature, released energy (E') was also estimated for several PAHs, such as phenanthrene, anthracene, pyrene, and coronene (Table S3). Comparison of released energy (E') and strain energy (E_s) calculated based on nonplanar distortions of the molecule[15,18] are described for the aforementioned PAHs, highlighting the unique nature of corannulene. Namely, corannulene has strain and released energies of 101.4 and 202.0 kJ/mol, respectively, that is significantly higher than for the selected PAHs. From another perspective, we have also investigated a family of extended carbon π-bowls such as cyclopenta[*bc*]corannulene ($C_{22}H_{10}$), dicyclopenta[*bc,ef*]corannulene ($C_{24}H_{10}$), tricyclopenta[*bc,ef,kl*]corannulene ($C_{26}H_{10}$), tetracyclopenta[*bc,ef,hi,kl*]corannulene ($C_{28}H_{10}$), and half-buckminsterfullerene ($C_{30}H_{10}$) which

also possess the curved geometry as corannulene molecule. Analysis of key factors such as strain energy[15] and estimated average released energy (Scheme S3 and Figure S10) for the carbon π-bowls revealed that all parameters are higher for the considered π-bowls than for corannulene (Table S4 and Scheme S3). For instance, half-buckminsterfullerene has a strain energy nearly four-fold higher (402 kJ/mol) than E_s of corannulene (101 kJ/mol, Table S4). Hydrogenation of C=C bond is more likely to be observed in the extended carbon π-bowls possessing even larger strain energy and released energy values compared to corannulene (Scheme S3). Therefore, the extended carbon π-bowls could be considered a class of compounds that undergo "unzipping" during a hydrogenation reaction due to high strain energy of the curved molecules.

Table S3. Strain energy (E_s)[15] and released energy (E') for several polycyclic aromatic hydrocarbons (PAHs). Released energy was calculated using the B3LYP/6-31+G* level of theory.

PAH	E_s, kJ/mol	E', kJ/mol
phenanthrene	0.0	135.7
anthracene	0.0	119.4
pyrene	0.0	129.1
coronene	0.0	123.4
corannulene	101.4	202.0

Table S4. Strain energy (E_s)[15] and average released energy (E'_{avg}) for several extended carbon π-bowls. Released energy was calculated using the B3LYP/6-31+G* level of theory.

extended carbon π-bowl	E_s, kJ/mol	E'_{avg}, kJ/mol
corannulene	101.4	202.0
cyclopenta[*bc*]corannulene	175.3	239.3
dicyclopenta[*bc,ef*]corannulene	238.8	400.0
tricyclopenta[*bc,ef,kl*]corannulene	300.5	419.7
tetracyclopenta[*bc,ef,hi,kl*]corannulene	352.0	537.9
half-buckminsterfullerene	401.6	664.4

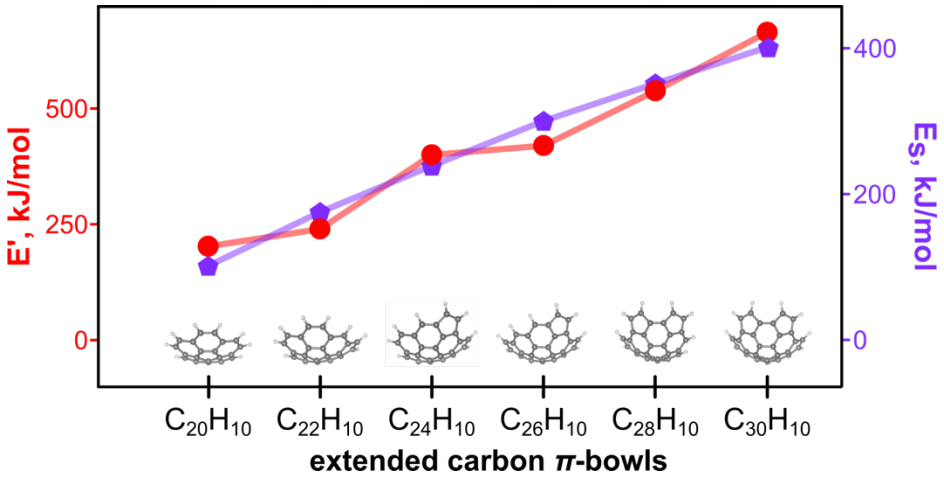

Scheme S3. E_s (purple)[15] and E' (red) as a function of carbon π-bowls for the PAHs: (*left to right*) corannulene ($C_{20}H_{10}$), cyclopenta[*bc*]corannulene ($C_{22}H_{10}$), dicyclopenta[*bc,ef*]corannulene ($C_{24}H_{10}$), tricyclopenta[*bc,ef,kl*]corannulene ($C_{26}H_{10}$), tetracyclopenta[*bc,ef,hi,kl*]corannulene ($C_{28}H_{10}$), and half-buckminsterfullerene ($C_{30}H_{10}$).

We have also examined optical excitations of isolated corannulene, "unzipped" corannulene (P-$C_{20}H_{14}$), TCNQ, and the relevant dimers, employing B3LYP-D3/6-311+G** with the dispersion correction in the direct TDDFT calculation. The dispersion correction and a large basis set are employed to produce a more accurate representation of the dimer excitations. The atomic positions for all of the dimers are taken from the experimental geometry of **1** and

(corannulene)$_2$·TCNQ co-crystals. Co-crystals of (corannulene)$_2$·TCNQ consist of two types of columns along the *c*-axis: one with an alternating column with a repeating unit of one corannulene and one TCNQ similar to alternation of P-$C_{20}H_{14}$ and TCNQ molecules in **1**. In the case of TCNQ/$C_{20}H_{10}$ dimer, we examined three mutual orientations of TCNQ and corannulene molecules: TCNQ/$C_{20}H_{10}$/TCNQ, $C_{20}H_{10}$/TCNQ, and TCNQ/$C_{20}H_{10}$ (Figure S8). The results from the electronic excitations analysis are in line with the experimentally observed red emission: the TCNQ/P-$C_{20}H_{14}$ "stack" is the only species with excitation energies of appreciable strength around 1.8 eV (690 nm). The lowest excitations for TCNQ, π-bowl, and P-$C_{20}H_{14}$ were estimated to be 3.0, 4.3, and 3.6 eV (413, 288, and 344 nm), respectively (Figure S7).

Moreover, the calculated optical band at 1.8 eV corresponding to the TCNQ/P-$C_{20}H_{14}$ "stack" is attributed to the transition between the HOMO-2 and LUMO that are localized mostly on P-$C_{20}H_{14}$ and TCNQ, respectively (Figure 2). Such behavior is indicative of charge transfer (CT) between P-$C_{20}H_{14}$ and TCNQ molecules. Moreover, the TCNQ/P-$C_{20}H_{14}$ "stack" exhibits a significant dipole moment of 3.01 D directed towards TCNQ, and an electrostatic charge of –0.134 |e| on TCNQ compared to 1.90 D and −0.070 |e| corresponding to TCNQ/$C_{20}H_{10}$ "stack". Such a result is in line with the experimental evidence. Using the Kistenmacher relationship,[19] the charge on the TCNQ molecules was evaluated based on crystallographic data of **1** and (corannulene)$_2$·TCNQ co-crystals[3]. In the case of **1**, the charge on TCNQ was estimated to be –0.84 and for (corannulene)$_2$·TCNQ co-crystals was found to be –0.20. To understand the effect that a curved molecule can have on charge transfer, we compared electron couplings (that is proportional to CT rate) of TCNQ/P-$C_{20}H_{14}$ and TCNQ/$C_{20}H_{10}$ "stacks". Following analysis reported by Shustova and co-workers,[20,21] the electron couplings are estimated, according to the Marcus theory shown in Eqn (S4).[22]

$$k = \frac{2\pi}{\hbar}\frac{|V_c|^2}{\sqrt{4\pi\lambda k_B T}} \cdot \exp\left(-\frac{(\lambda+\Delta G^0)^2}{4\lambda k_B T}\right) \sim |V_c|^2 \qquad \text{(S4)}$$

In Eqn (S4), k is charge transfer rate, λ is the reorganization energy of a system in response to "instantaneous" relocation of an electron from the donor to the acceptor, ΔG° is the difference in the energies of the initial and final states, V_c is the electron coupling constant, and T is the temperature. Eqn (S4) is applicable in the weak initial/final state coupling regime, $V_c << \lambda$. Within the simplest picture, the influence of the molecular environment on the donor and acceptor states

is neglected; the initial electronic state is $|\mathrm{i}\rangle = |\mathrm{D}^{-}\rangle \times |\mathrm{A}\rangle$, the final state is $|f\rangle = |D\rangle \times |A^{-}\rangle$, and the reorganization energy within the mean-field theory is estimated in Eqn (S5) as:

$$\lambda = \mathrm{E}_{\mathrm{D}}^{\mathrm{LUMO}} - \mathrm{E}_{\mathrm{A}^{-}}^{\mathrm{HOMO}} \qquad \text{(S5)}$$

The electron couplings have been estimated using the direct coupling method,[23–25] defined for Hartree-Fock (HF) theory of the electronic structure. While the accuracy of the HF energies is limited by its mean-field character, the couplings are known to be more sensitive to the quality of the basis set, rather than to the electron correlation.[24] Despite the different mutual orientation of TCNQ and corannulene molecules, electron couplings for TCNQ/P-$C_{20}H_{14}$ "stack" is higher than for TCNQ/$C_{20}H_{10}$ "stack" (Table S5 and Figure S8). In the case of TCNQ/$C_{20}H_{10}$/TCNQ geometry (Figure S8), electron coupling was estimated according to Eqn (S6).

$$\mathrm{V_c} = \sqrt{\mathrm{V_c^{(1)}} \cdot \mathrm{V_c^{(2)}}} \qquad \text{(S6)}$$

In Eq. (S5), $\mathrm{V_c^{(1)}}$ and $\mathrm{V_c^{(2)}}$ are electron couplings for $C_{20}H_{10}$/TCNQ and TCNQ/$C_{20}H_{10}$. Since electron coupling is related to electron transfer rate, we can surmise that there is likely an increased electron transfer rate as well.

Table S5. Electron couplings estimated by the direct coupling method for TCNQ/$C_{20}H_{10}$ "stack" with different mutual orientations and TCNQ/P-$C_{20}H_{14}$ "stack". The theory level is HF/6-31+G*.

electron coupling V_c, eV			
TCNQ/$C_{20}H_{10}$	$C_{20}H_{10}$/TCNQ	TCNQ/$C_{20}H_{10}$/TCNQ	TCNQ/P-$C_{20}H_{14}$
0.0011	0.0899	0.0099	0.1405

Neutral corannulene molecule, $C_{20}H_{10}$, has a bowl depth of 0.87 Å (measured from the plane of the hub carbon atoms to the plane of rim carbon atoms) with an energy barrier for π-bowl inversion through a planar transition state of ~40 kJ/mol. According to the electronic structure calculations, a π-bowl can accommodate up to 4 electrons into its doubly degenerate low-lying LUMO. This analysis is in agreement with experiments on corannulene layered with Li and Li/Cs, forming "sandwiches" of charged π-bowls "sprinkled" with metal ions.[16,17] Another doubly-degenerate orbital, LUMO+1 of energy –1.8 eV, may also contribute to the charge transfer properties and hydrogenation of the bond cleavage in corannulene. As shown in Table S6, addition of a negative charge flattens the π-bowl (measured from the plane of the hub carbon atoms to the

plane of rim carbon atoms) and stretches the maximum C–C bond along its rim up to 6%, thus lowering the inversion barrier to 25.4 kJ/mol for $C_{20}H_{10}^{2-}$. A similar trend of flattening of anionic bowls is reported in literature.[16,17] For example, in the iconic findings of Petrukhina and co-workers, the bowl depth of the corannulene tetraannion was 0.29 Å compared to 0.88 Å of pristine corannulene.[26] Interestingly, the presence of TCNQ in the reaction mixture also can affect the bowl flattering. For instance, in the alternating TCNQ/corannulene columns, the bowl depth of corannulene is reduced to 0.82 Å in comparison with that of parent corannulene (0.87 Å). The π-orbital axis vector (POAV) pyramidalization angle (another parameter for curvature estimation) was found to be 10% decreased for the alternating TCNQ/corannulene columns.[3] These properties of charged corannulene may contribute to the C–C bond cleavage and formation of P-$C_{20}H_{14}$, characterized by the planar geometry of the structure.

Table S6. The bowl depth, bowl-inversion barrier ($E^{\dagger}$), and the maximum and average distance between rim carbons ($d(C_{rim}\text{-}C_{rim})$) for an isolated corannulene molecule computed at B3LYP/6-31+G* level of the electronic structure theory. The electronic energies for optimized molecular geometries are used.

Charge	0	1–	2–
Bowl depth, Å	0.87	0.83	0.78
$E^{\dagger}$, kJ/mol	39.0	30.9	25.4
$d(C_{rim}{-}C_{rim})_{max}$, Å	1.383	1.426	1.460
$d(C_{rim}{-}C_{rim})_{avg}$, Å	1.383	1.408	1.425

Furthermore, we proposed that the transformation of a buckybowl, $C_{20}H_{10}$, to a planar moiety, P-$C_{20}H_{14}$, occurs in a series of concomitant reactions that is first initiated by a sequence of electron and proton transfers (Note that addition of a single electron to the species in Figure 1 creates stable anions). All geometries of intermediates ($C_{20}H_{11}^{\bullet}$, $C_{20}H_{12}$, and $C_{20}H_{13}^{\bullet}$) were optimized at the B3LYP/6-31+G* level of theory (Figures S11–S13). For $C_{20}H_{12}$, three isomers were determined (Figure S11) and for one isomer, a C–C bond was cleaved and radicals were delocalized on the carbon atoms of the methyl groups. We estimated that the electronic component for bond dissociation energy (E_{C-C}) in $C_{20}H_{12}$ is 115 kJ/mol, that serves as evidence of the weak

C–C bond. Moreover, an additional electron reduces E_{C-C} to 9 kJ/mol in $C_{20}H_{12}^{-\bullet}$. For example, in a $RCH_2–CH_2R$ system where R is a pyrene core then the electronic energy of a C–C bond was found to be ~360 kJ/mol (Figure S14) or if R belongs to a benzo[*ghi*]fluoranthene core that is present in $C_{20}H_{12}$ or $C_{20}H_{12}^{-\bullet}$ intermediates, E_{C-C} is estimated to be 224 kJ/mol (Figure S30). Thus, $C_{20}H_{12}$ and $C_{20}H_{12}^{-\bullet}$ intermediates have weaker C–C bonds that could potentially lead to C–C bond scission. We also probed two key driving forces of the C–C bond cleavage in $C_{20}H_{12}$ and $C_{20}H_{12}^{-\bullet}$: the aromaticity stabilization of formed radicals through delocalization over the conjugated aromatic system and strain energy release. As an analog of $C_{20}H_{12}$ without strain, we chose 1,2-dihydrocoronene ($C_{24}H_{14}$). The rationale of this choice is that $C_{20}H_{12}$ and $C_{24}H_{14}$ are derivatives of corannulene and coronene, respectively, that belong to one class of compounds – circulene. Another factor is that formed biradicals during C–C bond cleavage in both $C_{20}H_{12}$ and $C_{24}H_{14}$ are aromatic according to Hückel's rule (if cyclic hydrocarbons contain $4n+2$ π-electrons, it is aromatic), i.e., they contain 18 and 22 π-electrons, respectively. We estimated E_{C-C} for $C_{20}H_{12}$ and $C_{24}H_{14}$ as well as released energy (Figure S15). The bond dissociation energy of a C–C bond in $C_{24}H_{14}$ is 302 kJ/mol (360 kJ/mol for typical C–C bond)[27], which is over 2.5-fold stronger than the C–C bond found in $C_{20}H_{12}$ suggesting that the driving force of C–C bond scission in $C_{20}H_{12}$ is not aromaticity stabilization. The determined released energy attributed to strain in $C_{24}H_{14}$ is only 10.8 kJ/mol, 15-fold less than the energy released from the partially hydrogenated and significantly strained π-bowl, $C_{20}H_{12}$ (163 kJ/mol). Thus, we argue that the high strain energy as well as high released energy of corannulene is a key factor facilitating the planarization of corannulene.

In relation to the presented experiments, we have examined the optical transitions corresponding to the ground state, the first and the second excited singlet states of **X**, **X′**, and P-$C_{20}H_{14}$ employing the B3LYP-D3/6-31+G* method with the dispersion correction in the direct TDDFT calculation. While the electronic transition of the first excited singlet state for both **X** and **X′** do not differ from the optical transitions corresponding to the ground state (3.53 eV for **X** and 3.43 eV for **X′**), optical transitions for the second excited singlet states were determined to be 3.14 eV and 3.01 eV for **X** and **X′**, respectively (Figures S27 and S28). A diagram of the electronic transitions pathway, presented in Figure 4, is shown for the molecular model of the **X** and **X′** molecules in THF media; S_0 and S_2 refer to the structures optimized in the ground electronic state and S_0' and S_2' refer to the geometry optimized in the second excited singlet state. Absorption is associated with the optical transition from $S_0 \rightarrow S_2$, with the largest contributions coming from the

highest occupied natural transition orbital (HONTO) and lowest unoccupied natural transition orbital (LUNTO) of the ground state. Emission involves the $S_2' \rightarrow S_0'$ transition represented primarily by the LUNTO and HONTO of the second excited singlet state at the optimized geometry. Electronic transition analysis for P-$C_{20}H_{14}$ revealed that the optical transitions corresponding to the first and second excited singlet states have close energies 3.11 and 3.03 eV, respectively (Figure S29). That verifies that excited energy levels are more delocalized in P-$C_{20}H_{14}$ compared to corannulene analogs, **X** and **X′**. Overall, electronic transition structures are similar for broken corannulene, P-$C_{20}H_{14}$ (Figure 3), and its analogs, **X** and **X′** (Figure 4).

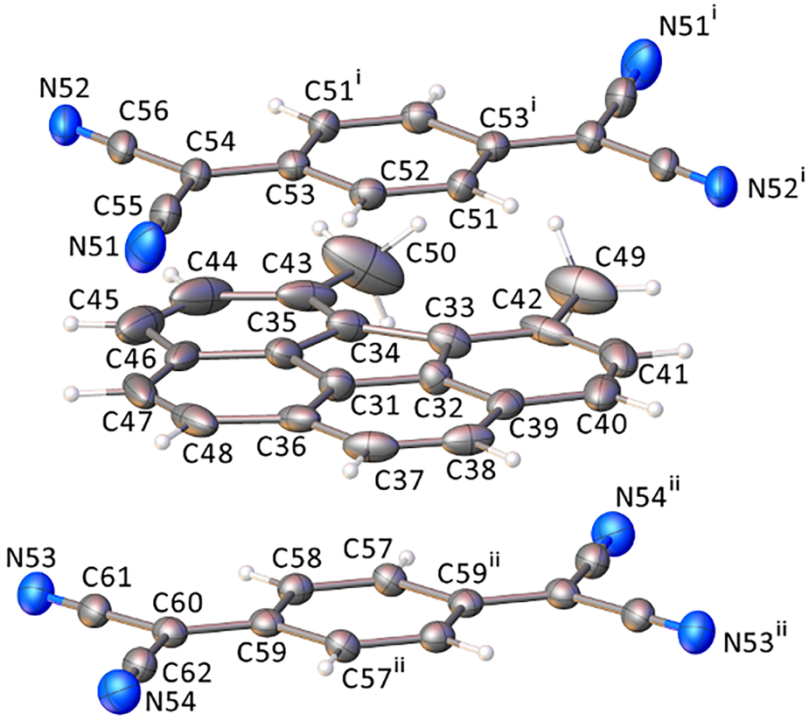

Figure S1. Crystal structure of **1**. Displacement ellipsoids drawn at the 40% probability level. Gray, blue, and white spheres correspond to carbon, nitrogen, and hydrogen atoms, respectively.

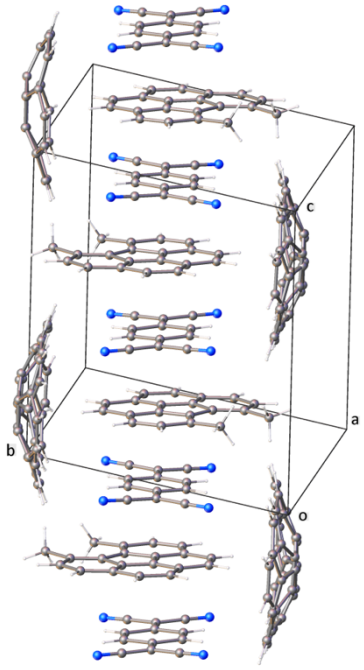

Figure S2. Packing of **1** along the *c*-axis highlighting TCNQ and P-$C_{20}H_{14}$ stacking. Gray, blue, and white spheres correspond to carbon, nitrogen, and hydrogen atoms, respectively.

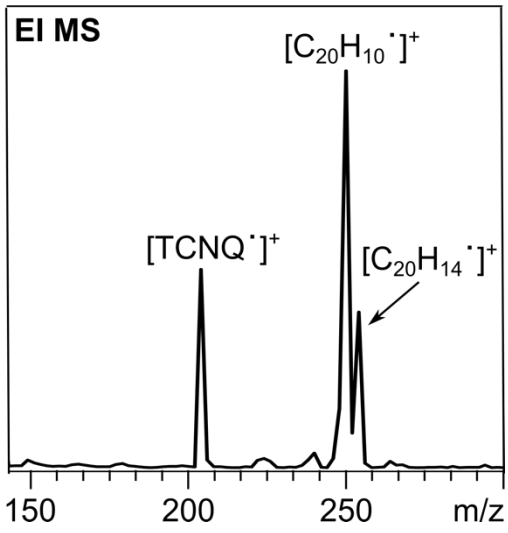

Figure S3. Mass spectrum of **1**.

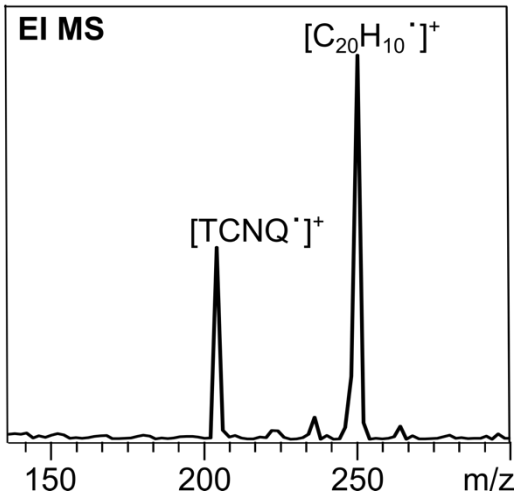

Figure S4. Mass spectrum of (corannulene)$_2$·TCNQ.

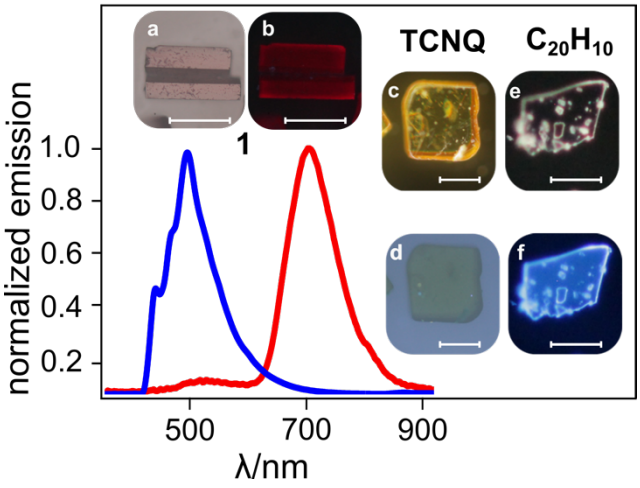

Figure S5. Normalized emission spectra of **1** (red) and corannulene ($C_{20}H_{10}$, blue) collected on corresponding single crystals. Epifluorescence images for single crystals of **1** (*a*), TCNQ (*c*), and $C_{20}H_{10}$ (*e*), and after λ_{ex} = 365 nm of **1** (*b*), TCNQ (*d*), and $C_{20}H_{10}$ (*f*). Scale bar represents 100 μm.

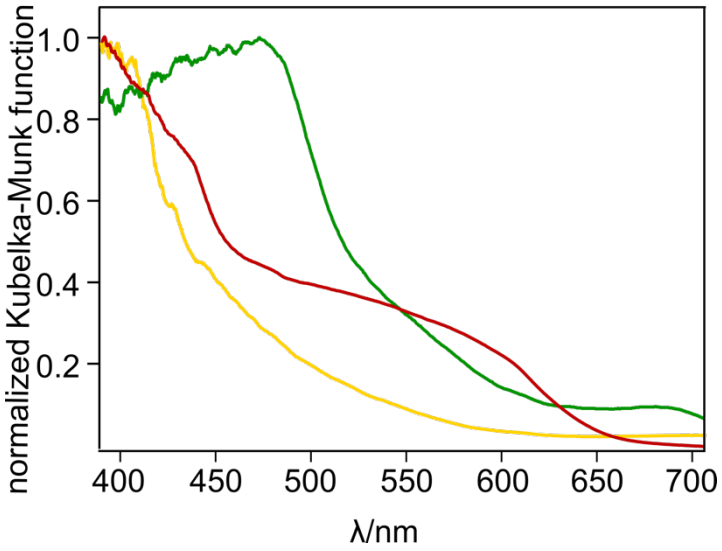

Figure S6. Normalized diffuse reflectance spectra of $C_{20}H_{10}$ (yellow), TCNQ (green), and **1** (red).

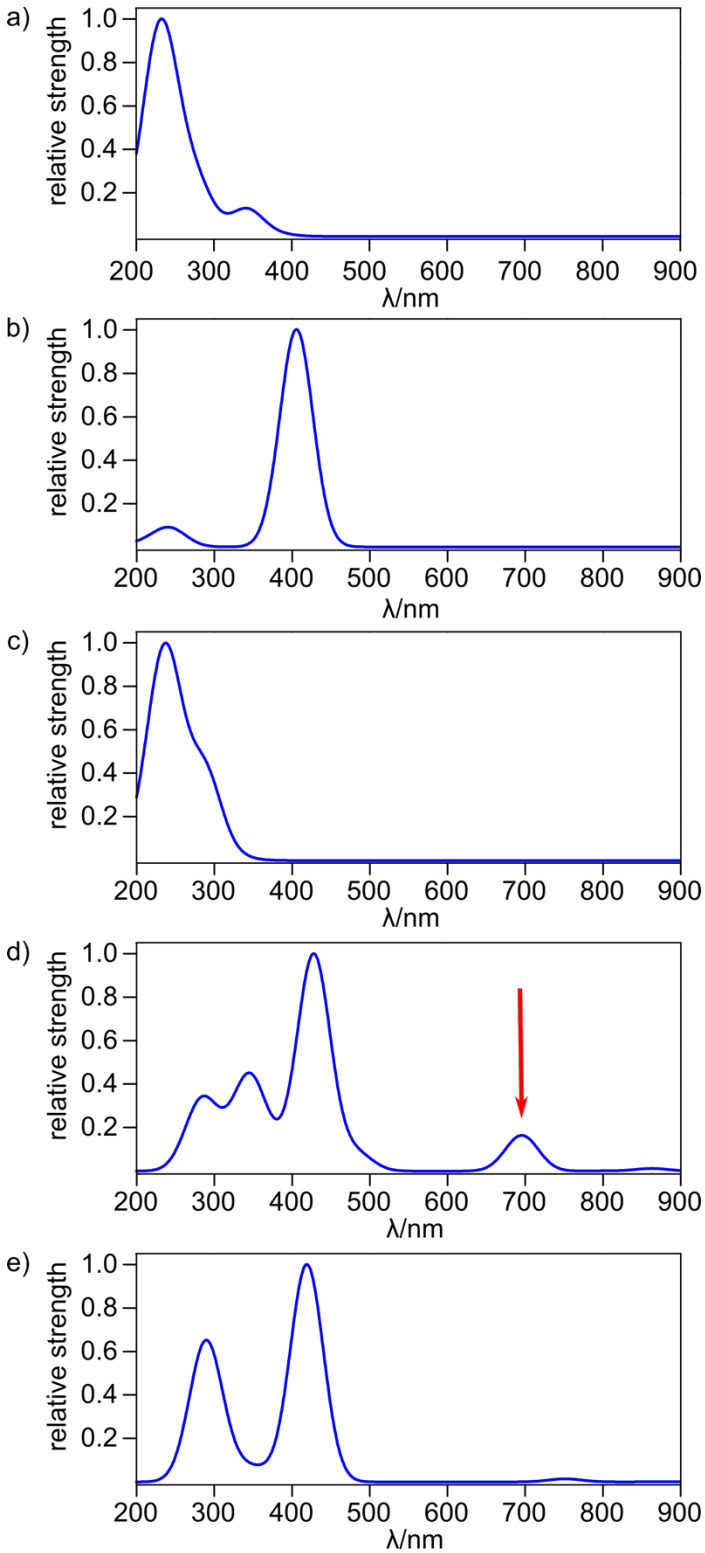

Figure S7. Optical transition strengths for the components of (*a*) P-$C_{20}H_{14}$, (*b*) TCNQ, (*c*) $C_{20}H_{10}$, (*d*) TCNQ/P-$C_{20}H_{14}$, (*e*) TCNQ/$C_{20}H_{10}$. The arrow marks the excitation in the region unique to the TCNQ/$C_{20}H_{10}$ dimer. The theory level is TDDFT/RPA based on B3LYP-D3/6-311+G**.

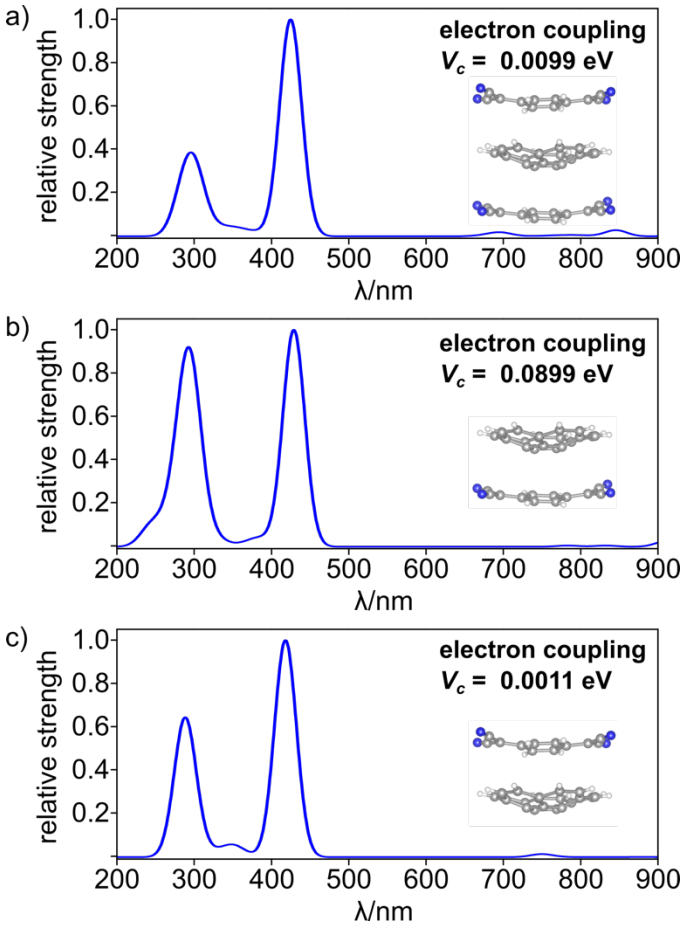

Figure S8. Optical transition strengths and the corresponding electron couplings for TCNQ/$C_{20}H_{10}$ "stack" with different mutual orientations: (*a*) TCNQ/$C_{20}H_{10}$/TCNQ, (*b*) $C_{20}H_{10}$/TCNQ, and (*c*) TCNQ/$C_{20}H_{10}$. The theory level is TDDFT/RPA based on B3LYP-D3/6-311+G.

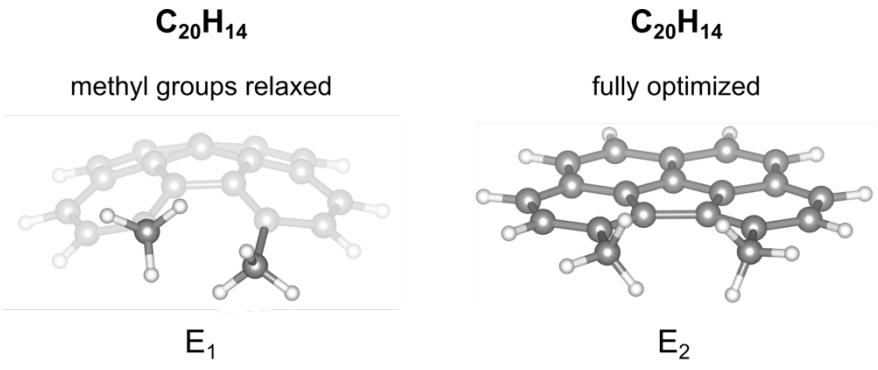

Figure S9. Schematic representation of the technique for calculating the electronic component of released energy (*E'*) during planarization of $C_{20}H_{14}$. Highlighted are the atoms which positions were optimized. The theory level is B3LYP/6-31+G* as implemented in QChem 5.2.[14]

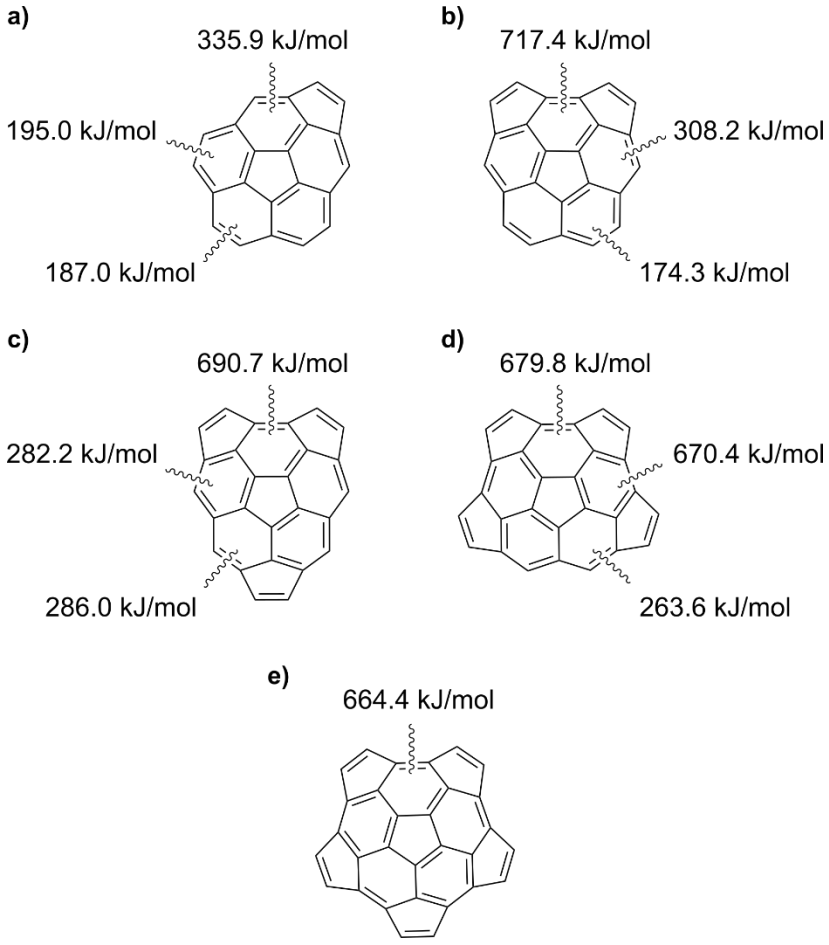

Figure S10. Released energy (*E*′) estimated for the cleavage of various C=C bond in: (*a*) cyclopenta[*bc*]corannulene, (*b*) dicyclopenta[*bc,ef*]corannulene, (*c*) tricyclopenta[*bc,ef,kl*]corannulene, (*d*) tetracyclopenta[*bc,ef,hi,kl*]corannulene, and (*e*) half-buckminsterfullerene. The average *E*′ can be found in Table S5.

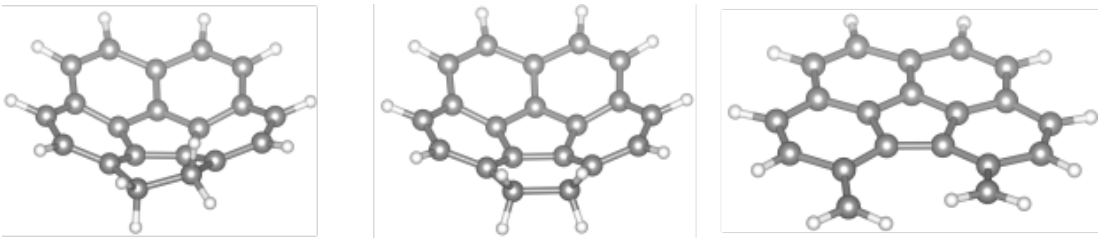

Figure S11. (*left to right*) Optimized geometries of three $C_{20}H_{12}$ isomers. The theory level is CCSD/cc-pVDZ.

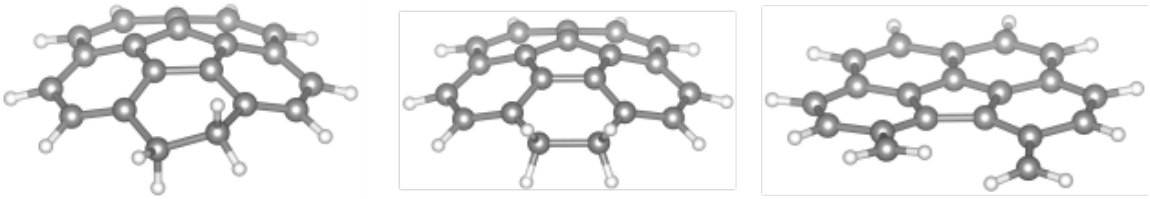

Figure S12. (*left to right*) Optimized geometries of three $C_{20}H_{12}^{-\bullet}$ isomers. The theory level is CCSD/cc-pVDZ.

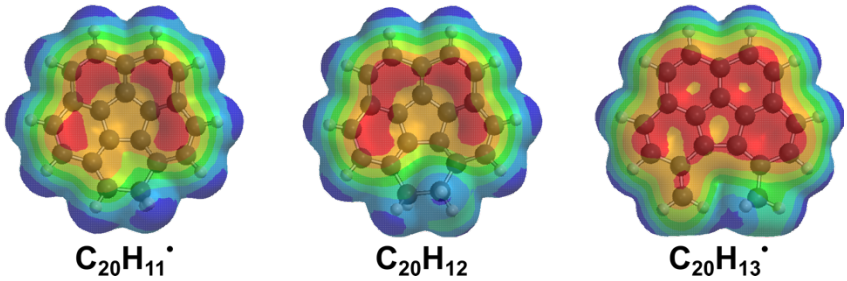

Figure S13. (*left to right*) Optimized geometries and molecular electrostatic potential (MEP) maps of $C_{20}H_{11}^{\bullet}$, $C_{20}H_{12}$, and $C_{20}H_{13}^{\bullet}$. The theory level is B3LYP/6-31+G* (isovalue = 0.002 a.u.).

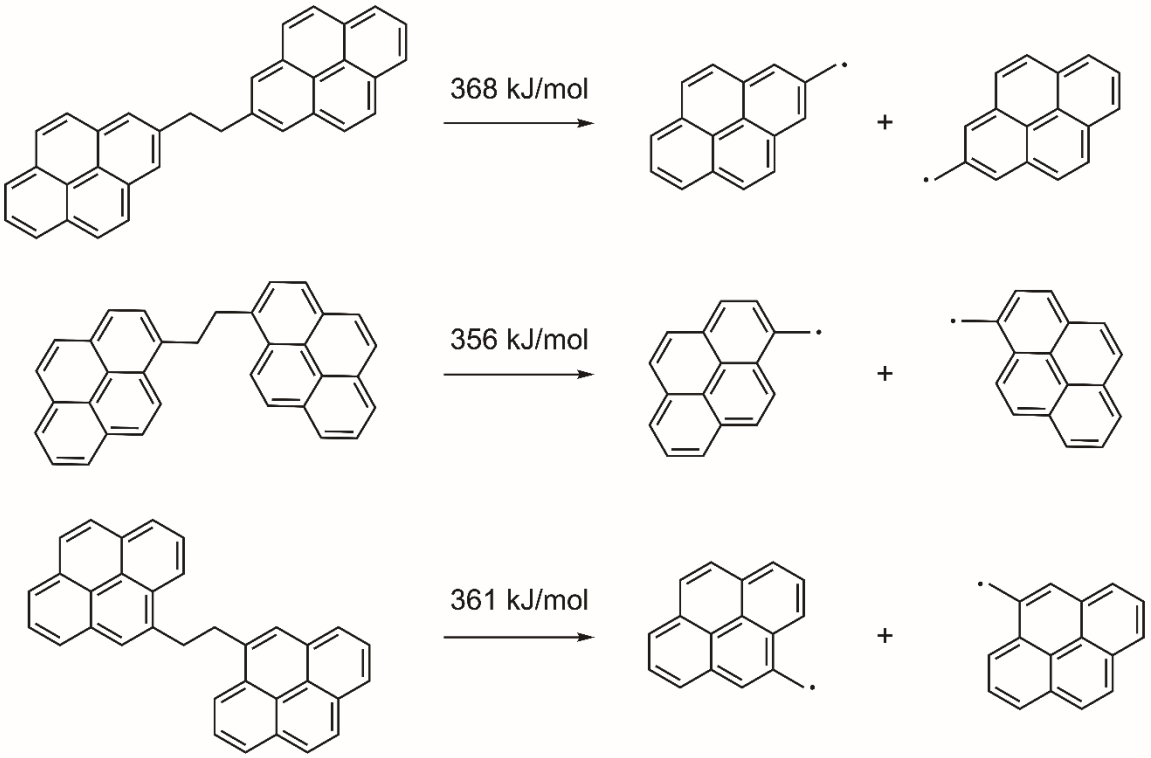

Figure S14. Estimation of the electronic component of $E_{C–C}$ in $RCH_2–CH_2R$ with R belonging to a pyrene core. The theory level is B3LYP/6-31+G*.

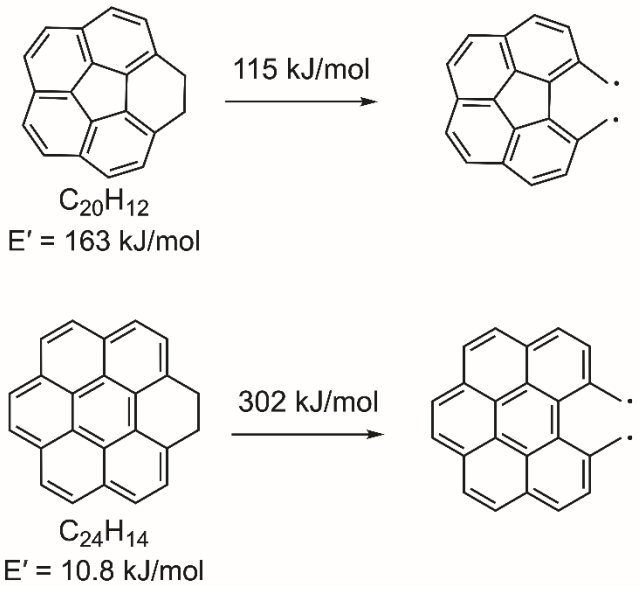

Figure S15. Estimation of the electronic component of $E_{C–C}$ and released energy in $C_{20}H_{12}$ and $C_{24}H_{14}$. The theory level is B3LYP/6-31+G*.

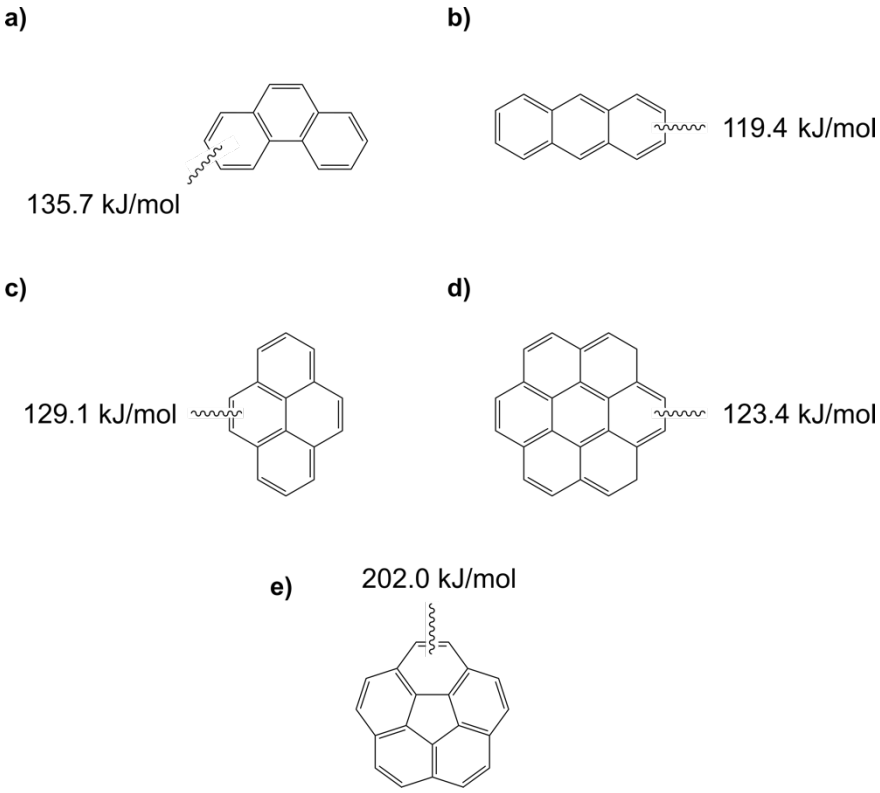

Figure S16. Released energy (*E*′) estimated for the cleavage of various C=C bond in: (*a*) phenanthrene, (*b*) anthracene, (*c*) pyrene, (*d*) coronene, and (*e*) corannulene. The average *E*′ can be found in Tablea S4.

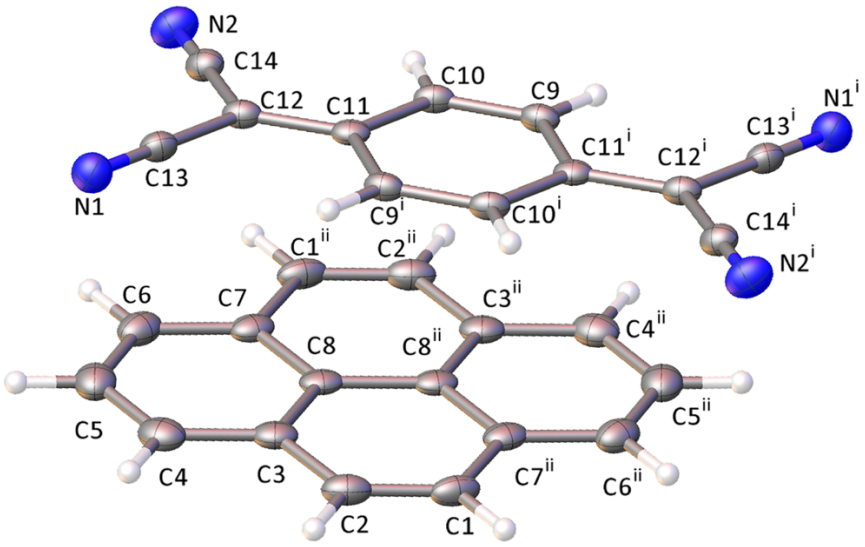

Figure S17. Crystal structure of $C_{16}H_{10}$·$C_{12}H_4N_4$ (pyr·TCNQ). Displacement ellipsoids drawn at the 50% probability level. Gray, blue, and white spheres correspond to carbon, nitrogen, and hydrogen atoms, respectively.

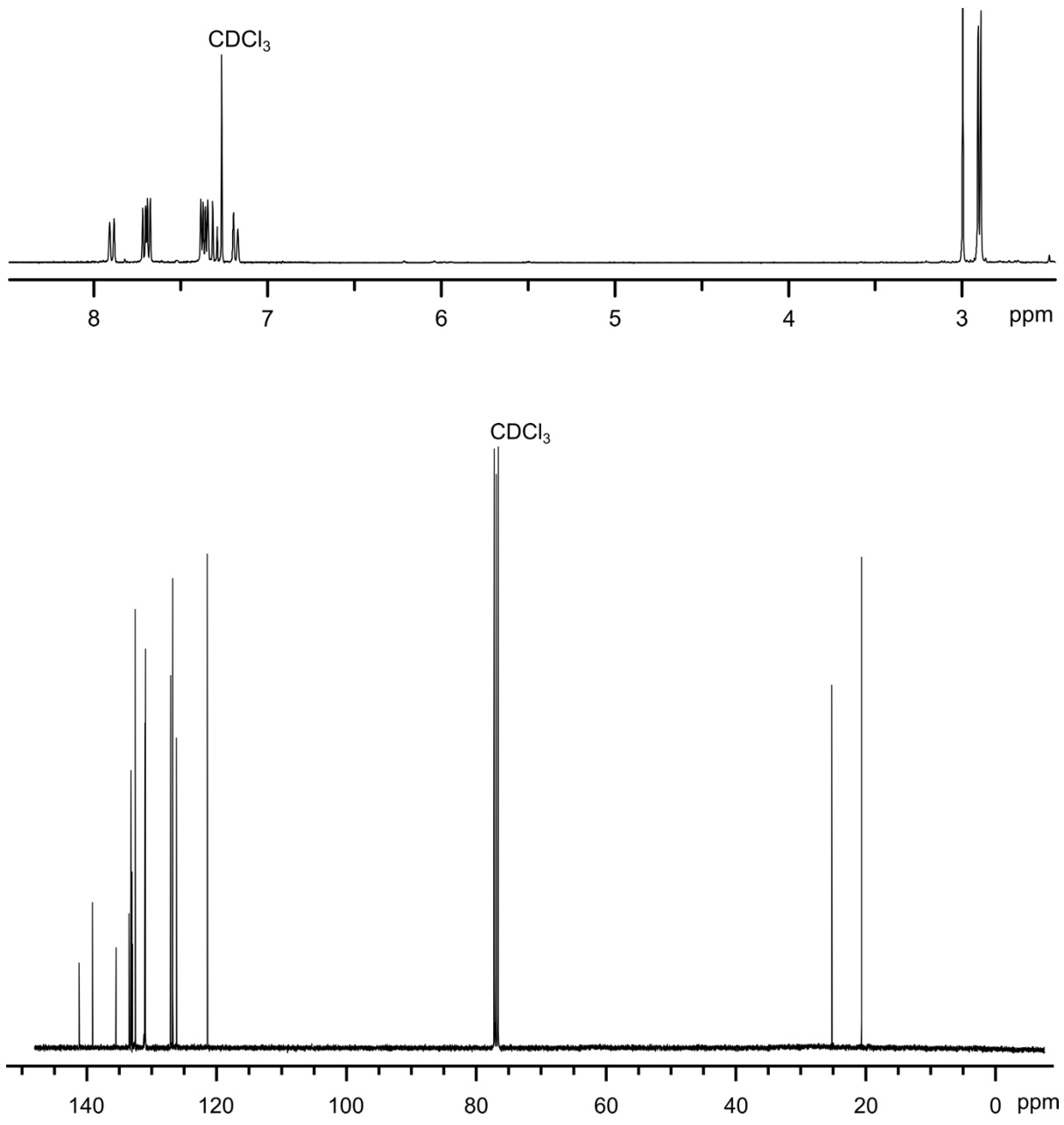

Figure S18. ^{1}H NMR and ^{13}C NMR spectra of 1,6,7-trimethylfluoranthene (Scheme 1, compound **VII**).

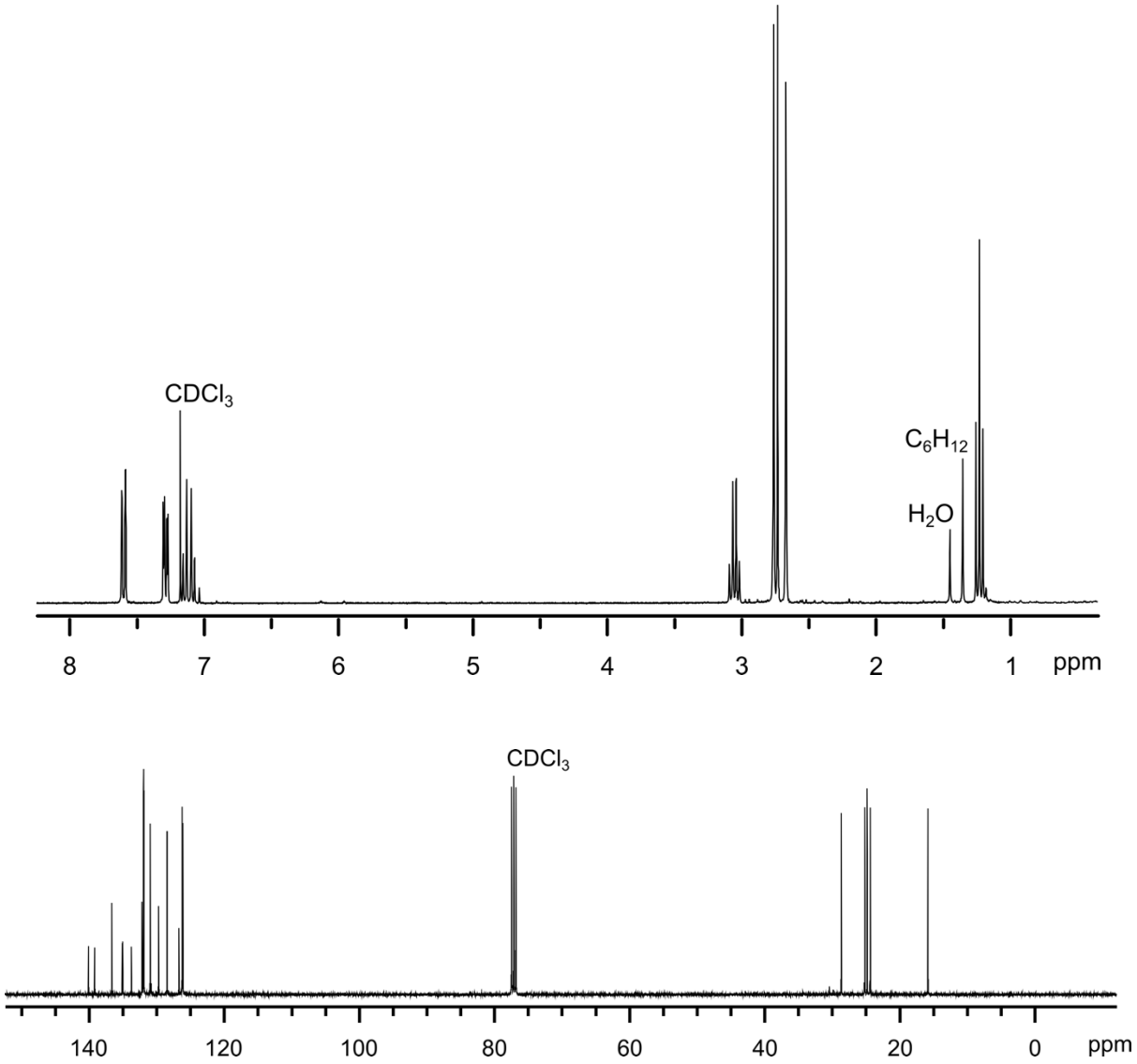

Figure S19. ^{1}H NMR and ^{13}C NMR spectra of 7-ethyl-1,6,10-trimethylfluoranthene (Scheme 2, compound **VII′**).

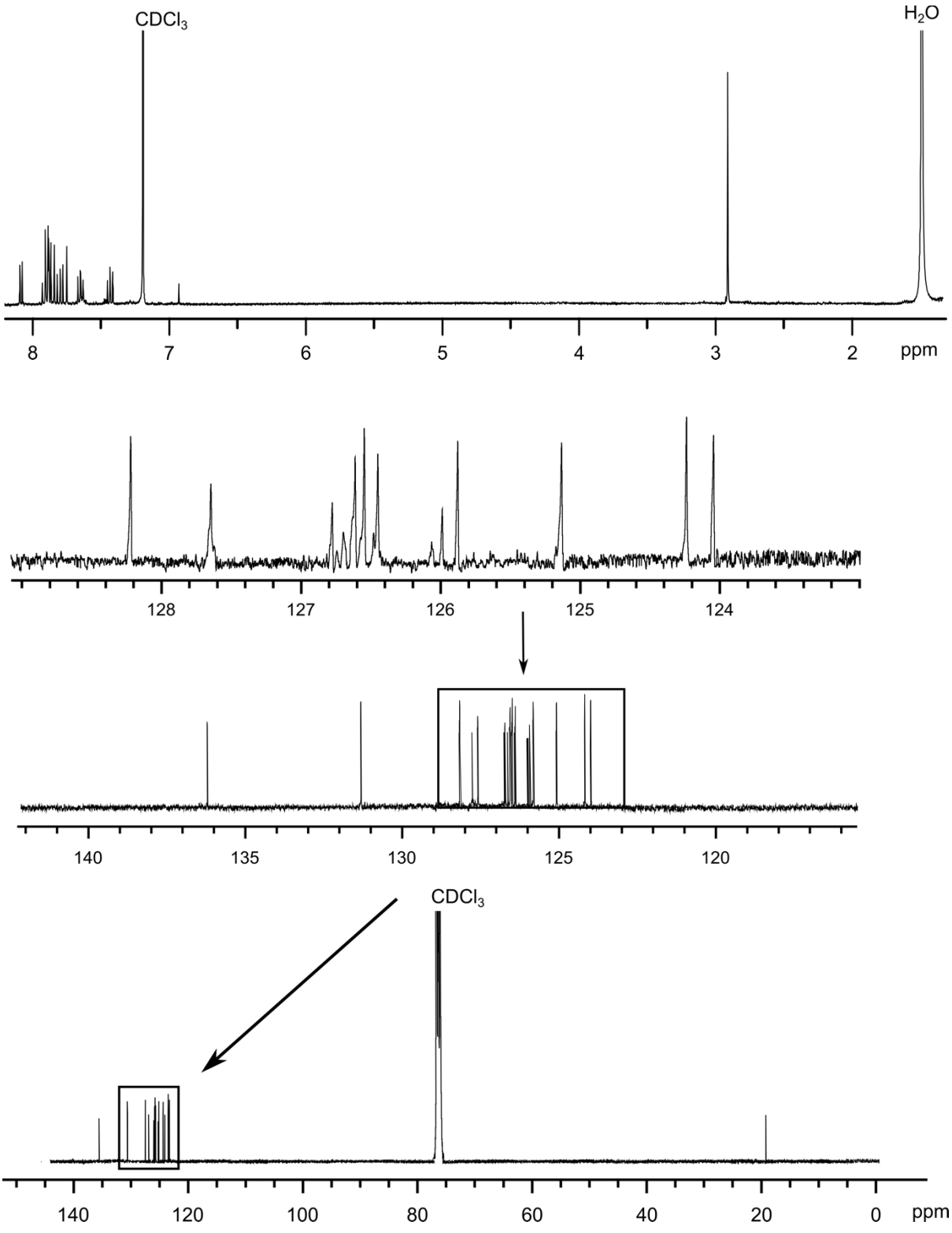

Figure S20. ^{1}H NMR and ^{13}C NMR spectra of 5-methylbenzo[*ghi*]fluoranthene (Scheme 1, compound **X**).

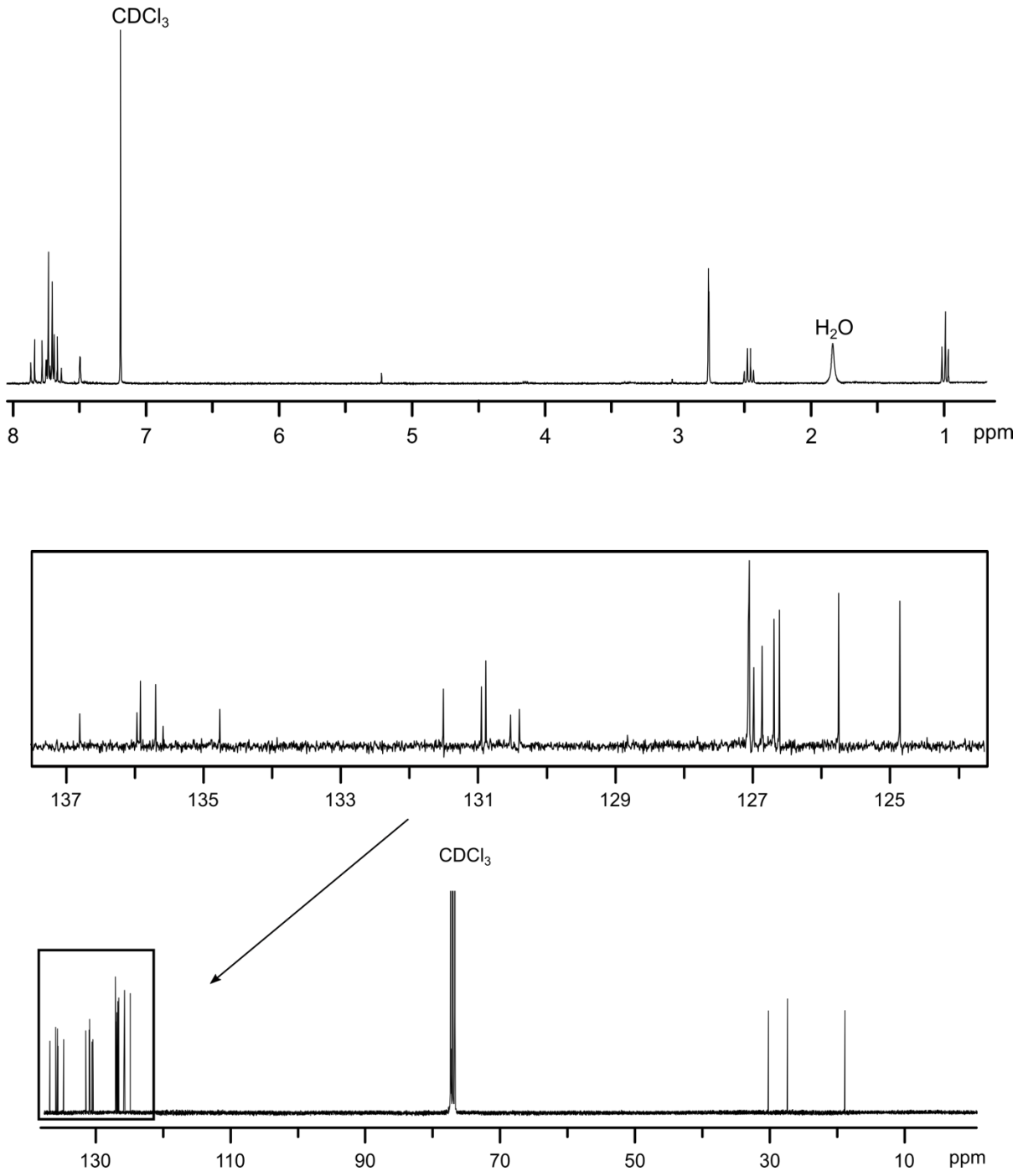

Figure S21. ^{1}H NMR and ^{13}C NMR spectra of 5-ethyl-6-methylbenzo[*ghi*]fluoranthene (Scheme 2, compound **X′**).

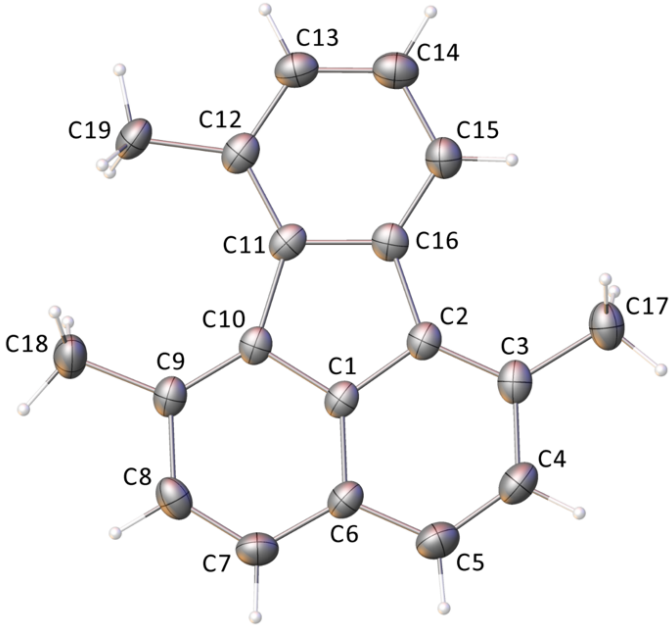

Figure S22. Crystal structure of 1,6,7-trimethylfluoranthene ($C_{19}H_{16}$, Scheme 1, compound **VII**). Displacement ellipsoids drawn at the 50% probability level. Gray and white spheres correspond to carbon, and hydrogen atoms, respectively.

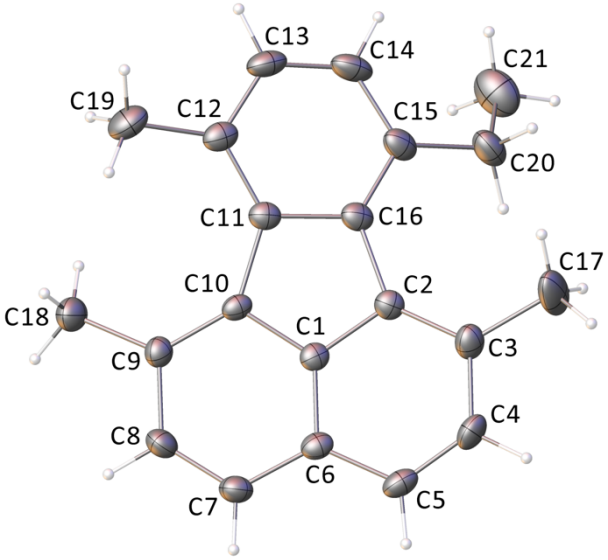

Figure S23. Crystal structure of 7-ethyl-1,6,10-trimethylfluoranthene ($C_{21}H_{10}$, Scheme 2, compound **VII′**). Displacement ellipsoids drawn at the 50% probability level. Gray and white spheres correspond to carbon, and hydrogen atoms, respectively.

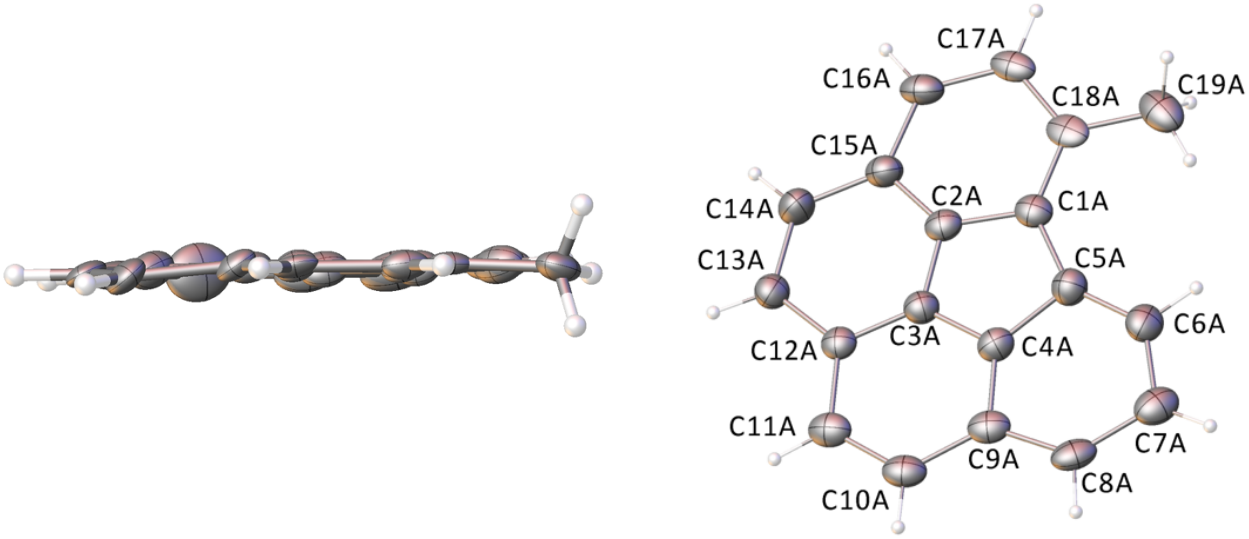

Figure S24. Crystal structure of 5-methylbenzo[*ghi*]fluoranthene ($C_{19}H_{12}$, Scheme S1, compound **X**). Displacement ellipsoids drawn at the 20% probability level. Gray and white spheres correspond to carbon, and hydrogen atoms, respectively.

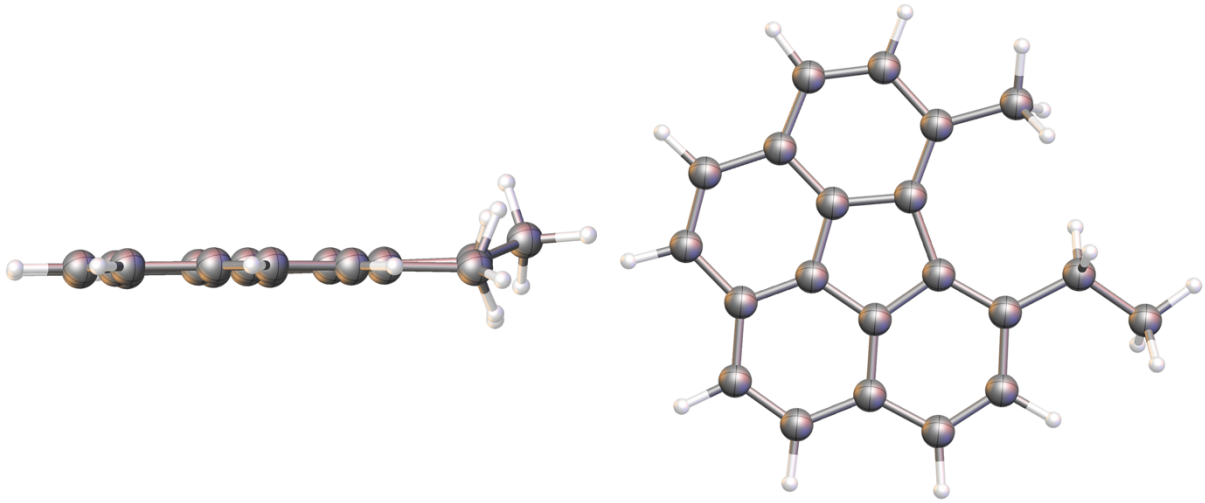

Figure S25. Optimized structure of 5-ethyl-6-methylbenzo[*ghi*]fluoranthene ($C_{21}H_{16}$, Scheme S2, compound **X′**) based on the B3LYP-D3/6-31+G* level of theory. Gray and white spheres correspond to carbon, and hydrogen atoms, respectively.

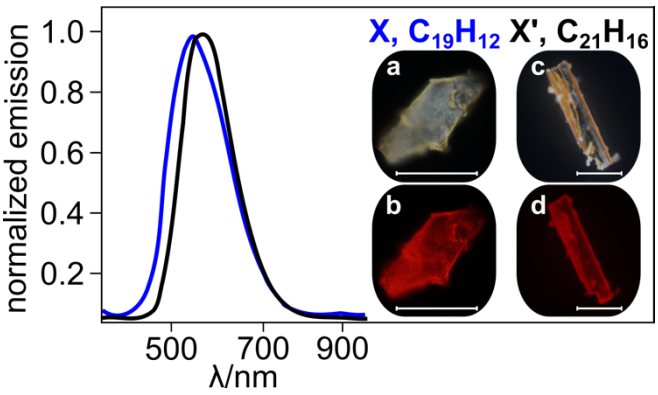

Figure S26. Normalized emission spectra of **X** (blue) and **X′** (black) collected on corresponding single crystals. Scale bar represents 50 μm.

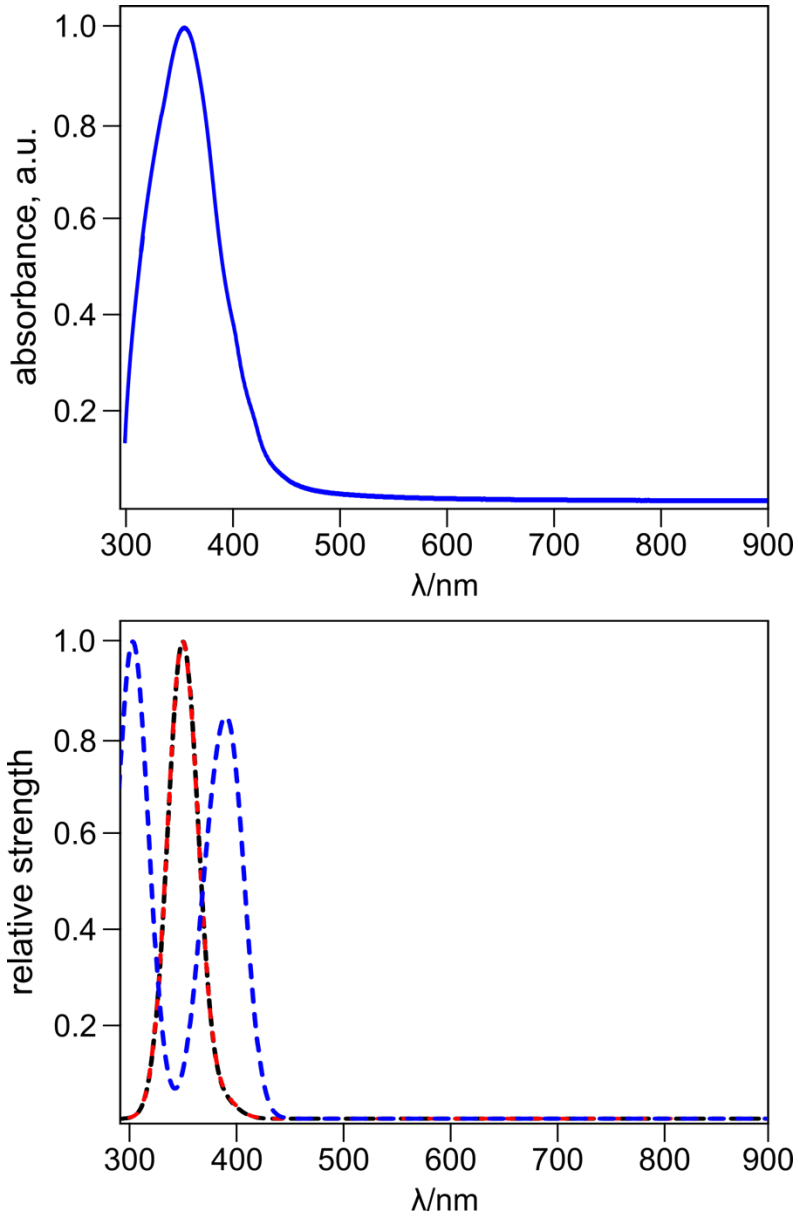

Figure S27. (*top*) Normalized absorbance spectrum of 5-methylbenzo[*ghi*]fluoranthene (**X**) in THF. (*bottom*) Optical transition strengths computed at the ground state optimal geometry for **X** in THF (black), at the first excited singlet state optimal geometry for **X** in THF (red), and at the second excited singlet state optimal geometry for **X** in THF (blue). The theory level is TDDFT/RPA based on B3LYP-D3/6-31+G*.

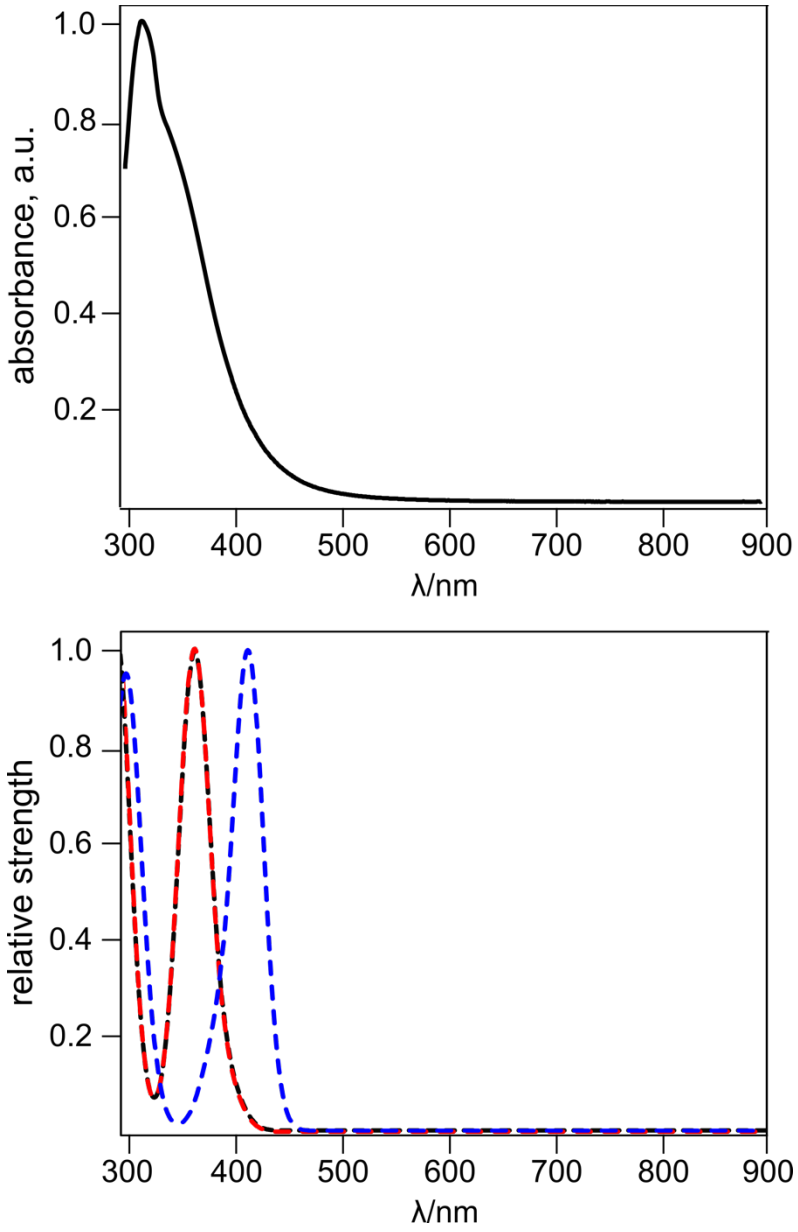

Figure S28. (*top*) Normalized absorbance spectrum of 5-ethyl-6-methylbenzo[*ghi*]fluoranthene (**X′**) in THF. (*bottom*) Optical transition strengths computed at the ground state optimal geometry for **X′** in THF (black), at the first excited singlet state optimal geometry for **X′** in THF (red), and at the second excited singlet state optimal geometry for **X′** in THF (blue). The theory level is TDDFT/RPA based on B3LYP-D3/6-31+G*.

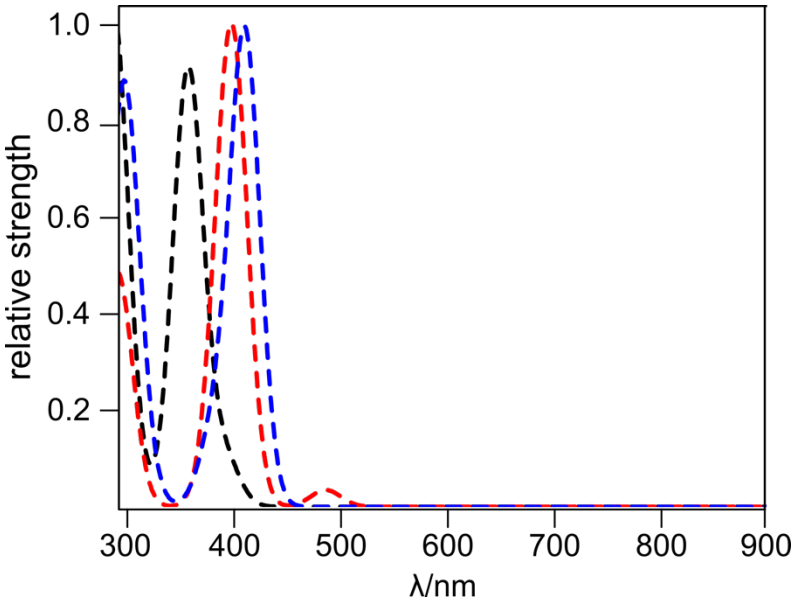

Figure S29. Optical transition strengths computed at the ground state optimal geometry for P-$C_{20}H_{14}$ in THF (black), at the first excited singlet state optimal geometry for P-$C_{20}H_{14}$ in THF (red), and at the second excited singlet state optimal geometry for P-$C_{20}H_{14}$ in THF (blue). The theory level is TDDFT/RPA based on B3LYP-D3/6-31+G*.

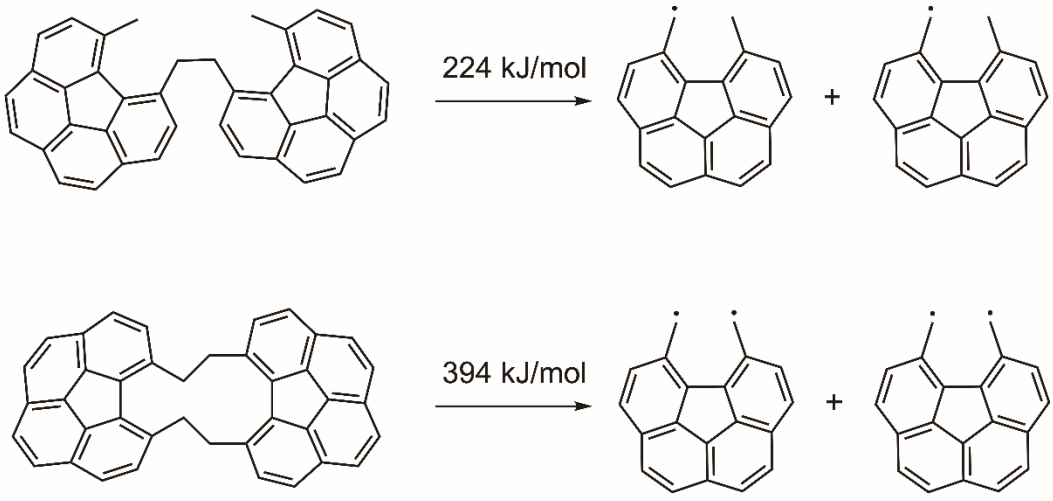

Figure S30. Estimation of the electronic component of $E_{C–C}$ in $RCH_2–CH_2R$ with R belonging to a benzo[*ghi*]fluoranthene core. The theory level is B3LYP/6-31+G*.

References:

1 A. M. Butterfield, B. Gilomen and J. S. Siegel, *Org. Process Res. Dev.*, 2012, **16**, 664–676.

2 C. Dallaire, I. Kolber and M. Gingras, *Org. Synth.* 2002, **78**, 42–50.

3 Y. Yoshida, K. Isomura, Y. Nakamura, H. Kishida and G. Saito, *Chem. Lett.*, 2015, **44**, 709–711.

4 M. A. Dobrowolski, G. Garbarino, M. Mezouar, A. Ciesielski and M. K. Cyrański, *CrystEngComm*, 2014, **16**, 415–429.

5 K. K. Park, C. H. Oh and W. K. Joung, *Tetrahedron Lett.*, 1993, **34**, 7445–7446.

6 Y. Li, L. Yang, X. Chen, S. Niu, S. Ban, X. Feng and Q. Li, *ChemistrySelect*, 2019, **4**, 171–174.

7 B. K. Peters, K. X. Rodriguez, S. H. Reisberg, S. B. Beil, D. P. Hickey, Y. Kawamata, M. Collins, J. Starr, L. Chen, S. Udyavara, K. Klunder, T. J. Gorey, S. L. Anderson, M. Neurock, S. D. Minteer and P. S. Baran, *Science.*, 2019, **363**, 838–845.

8 G. M. Sheldrick, *Acta Crystallogr. Sect. A Found. Crystallogr.*, 2015, **71**, 3–8.

9 G. M. Sheldrick, *Acta Crystallogr. Sect. C Struct. Chem.*, 2015, **71**, 3–8.

10 O. V. Dolomanov, L. J. Bourhis, R. J. Gildea, J. A. K. Howard and H. Puschmann, *J. Appl. Crystallogr.*, 2009, **42**, 339–341.

11 L. Krause, R. Herbst-Irmer, G. M. Sheldrick and D. Stalke, *J. Appl. Crystallogr.*, 2015, **48**, 3–10.

12 S. Grimme, J. Antony, S. Ehrlich and H. Krieg, *J. Chem. Phys.*, 2010, **132**, 154104.

13 Y. Shao, L. F. Molnar, Y. Jung, J. Kussmann, C. Ochsenfeld, S. T. Brown, A. T. B. Gilbert, L. V. Slipchenko, S. V. Levchenko, D. P. O'Neill, R. A. DiStasio, Jr., R. C. Lochan, T. Wang, G. J. O. Beran, N. A. Besley, J. M. Herbert, C. Y. Lin, T. Van Voorhis, S. H. Chien, A. Sodt, R. P. Steele, V. A. Rassolov, P. E. Maslen, P. P. Korambath, R. D. Adamson, B. Austin, J. Baker, E. F. C. Byrd, H. Dachsel, R. J. Doerksen, A. Dreuw, B. D. Dunietz, A. D. Dutoi, T. R. Furlani, S. R. Gwaltney, A. Heyden, S. Hirata, C.-P. Hsu, G. Kedziora, R. Z. Khalliulin, P. Klunzinger, A. M. Lee, M. S. Lee, W. Z. Liang, I. Lotan, N. Nair, B. Peters, E. I. Proynov, P. A. Pieniazek, Y. M. Rhee, J. Ritchie, E. Rosta, C. D. Sherrill, A. C. Simmonett, J. E. Subotnik, H. Lee Woodcock, W. Zhang, A. T. Bell, A. K. Chakraborty, D. M. Chipman, F. J. Keil, A. Warshel, W. J. Hehre, H. F. Schaefer, J. Kong, A. I. Krylov, P. M. W. Gill and M. Head-Gordon, *Phys. Chem. Chem. Phys.*, 2006, **8**, 3172–3191.

14 Y. Shao, Z. Gan, E. Epifanovsky, A. T. B. Gilbert, M. Wormit, J. Kussmann, A. W. Lange, A. Behn, J. Deng, X. Feng, D. Ghosh, M. Goldey, P. R. Horn, L. D. Jacobson, I. Kaliman, R. Z. Khaliullin, T. Kuś, A. Landau, J. Liu, E. I. Proynov, Y. M. Rhee, R. M. Richard, M. A. Rohrdanz, R. P. Steele, E. J. Sundstrom, H. L. Woodcock, P. M. Zimmerman, D. Zuev, B. Albrecht, E. Alguire, B. Austin, G. J. O. Beran, Y. A. Bernard, E. Berquist, K. Brandhorst, K. B. Bravaya, S. T. Brown, D. Casanova, C.-M. Chang, Y. Chen, S. H. Chien, K. D. Closser, D. L. Crittenden, M. Diedenhofen, R. A. DiStasio, H. Do, A. D. Dutoi, R. G. Edgar, S. Fatehi, L. Fusti-Molnar, A. Ghysels, A. Golubeva-Zadorozhnaya, J. Gomes, M.

W. D. Hanson-Heine, P. H. P. Harbach, A. W. Hauser, E. G. Hohenstein, Z. C. Holden, T.-C. Jagau, H. Ji, B. Kaduk, K. Khistyaev, J. Kim, J. Kim, R. A. King, P. Klunzinger, D. Kosenkov, T. Kowalczyk, C. M. Krauter, K. U. Lao, A. D. Laurent, K. V. Lawler, S. V. Levchenko, C. Y. Lin, F. Liu, E. Livshits, R. C. Lochan, A. Luenser, P. Manohar, S. F. Manzer, S.-P. Mao, N. Mardirossian, A. V. Marenich, S. A. Maurer, N. J. Mayhall, E. Neuscamman, C. M. Oana, R. Olivares-Amaya, D. P. O'Neill, J. A. Parkhill, T. M. Perrine, R. Peverati, A. Prociuk, D. R. Rehn, E. Rosta, N. J. Russ, S. M. Sharada, S. Sharma, D. W. Small, A. Sodt, T. Stein, D. Stück, Y.-C. Su, A. J. W. Thom, T. Tsuchimochi, V. Vanovschi, L. Vogt, O. Vydrov, T. Wang, M. A. Watson, J. Wenzel, A. White, C. F. Williams, J. Yang, S. Yeganeh, S. R. Yost, Z.-Q. You, I. Y. Zhang, X. Zhang, Y. Zhao, B. R. Brooks, G. K. L. Chan, D. M. Chipman, C. J. Cramer, W. A. Goddard, M. S. Gordon, W. J. Hehre, A. Klamt, H. F. Schaefer, M. W. Schmidt, C. D. Sherrill, D. G. Truhlar, A. Warshel, X. Xu, A. Aspuru-Guzik, R. Baer, A. T. Bell, N. A. Besley, J.-D. Chai, A. Dreuw, B. D. Dunietz, T. R. Furlani, S. R. Gwaltney, C.-P. Hsu, Y. Jung, J. Kong, D. S. Lambrecht, W. Z. Liang, C. Ochsenfeld, V. A. Rassolov, L. V. Slipchenko, J. E. Subotnik, T. Van Voorhis, J. M. Herbert, A. I. Krylov, P. M. W. Gill and M. Head-Gordon, *Mol. Phys.*, 2015, **113**, 184–215.

15 C. H. Sun, G. Q. Lu and H. M. Cheng, *J. Phys. Chem. B*, 2006, **110**, 4563–4568.

16 R. C. Haddon and L. T. Scott, *Pure & Appl. Chem.*, 1986, **58**, 137–142.

17 S. N. Spisak, Z. Wei and M. A. Petrukhina, *Dalton Trans.*, 2017, **46**, 5625–5630.

18 C. H. Sun, D. Yao, G. Q. Lu and H. M. Cheng, *Chem. Phys. Lett.*, 2007, **434**, 160–164.

19 T. J. Kistenmacher, T. J. Emge, A. N. Bloch and D. O. Cowan, *Acta Crystallogr. Sect. B Struct. Crystallogr. Cryst. Chem.*, 1982, **38**, 1193–1199.

20 A. M. Rice, E. A. Dolgopolova, B. J. Yarbrough, G. A. Leith, C. R. Martin, K. S. Stephenson, R. A. Heugh, A. J. Brandt, D. A. Chen, S. G. Karakalos, M. D. Smith, K. B. Hatzell, P. J. Pelechia, S. Garashchuk, N. B. Shustova, P. J. Pellechia, S. Garashchuk and N. B. Shustova, *Angew. Chem. Int. Ed.*, 2018, **57**, 11310–11315.

21 G. A. Leith, A. M. Rice, B. J. Yarbrough, A. A. Berseneva, R. T. Ly, C. N. Buck, D. Chusov, A. J. Brandt, D. A. Chen, B. W. Lamm, M. Stefik, K. S. Stephenson, M. D. Smith, A. K. Vannucci, P. J. Pellechia, S. Garashchuk and N. B. Shustova, *Angew. Chem. Int. Ed.*, 2020, **59**, 6000–6006.

22 K. M. Pelzer, Á. Vázquez-Mayagoitia, L. E. Ratcliff, S. Tretiak, R. A. Bair, S. K. Gray, T. Van Voorhis, R. E. Larsen and S. B. Darling, *Chem. Sci.*, 2017, **8**, 2597–2609.

23 Z.-Q. You, C.-P. Hsu and G. R. Fleming, *J. Chem. Phys.*, 2006, **124**, 044506.

24 C.-H. Yang and C.-P. Hsu, *J. Chem. Phys.*, 2006, **124**, 244507.

25 Z.-Q. You, Y. Shao and C.-P. Hsu, *Chem. Phys. Lett.*, 2004, **390**, 116–123.

26 A. V. Zabula, A. S. Filatov, S. N. Spisak, A. Y. Rogachev and M. A. Petrukhina, *Science.*, 2011, **333**, 1008–1011.

27 S. J. Blanksby and G. B. Ellison, *Acc. Chem. Res.*, 2003, **36**, 255–263.